The fate of pyruvate dictates cell growth by modulating cellular redox potential

Ashish G. Toshniwal[1], Geanette Lam[1], Alex J. Bott[1], Ahmad A. Cluntun[1, 5], Rachel Skabelund[1], Hyuck-Jin Nam[2], Dona R. Wisidagama[2], Carl S. Thummel[2] and Jared Rutter[1, 3, 4]

Affiliations:

[1] Department of Biochemistry, University of Utah, Salt Lake City, UT 84132, USA

[2] Department of Human Genetics, University of Utah, Salt Lake City, UT 84132, USA

[3] Howard Hughes Medical Institute, University of Utah School of Medicine, Salt Lake City, UT 84132, USA

[4] Lead Contact

[5] Present address: Department of Biochemistry & Molecular Biology, Rutgers Robert Wood Johnson Medical School, Piscataway, NJ 08854

Abstract

Pyruvate occupies a central node in carbohydrate metabolism such that how it is produced and consumed can optimize a cell for energy production or biosynthetic capacity. This has been primarily studied in proliferating cells, but observations from the post-mitotic *Drosophila* fat body led us to hypothesize that pyruvate fate might dictate the rapid cell growth observed in this organ during development. Indeed, we demonstrate that augmented mitochondrial pyruvate import prevented cell growth in fat body cells *in vivo* as well as in cultured mammalian hepatocytes and human hepatocyte-derived cells *in vitro*. We hypothesize that this effect on cell size was caused by an increase in the $NADH/NAD^+$ ratio, which rewired metabolism toward gluconeogenesis and suppressed the biomass-supporting glycolytic pathway. Amino acid synthesis was decreased, and the resulting loss of protein synthesis prevented cell growth. Surprisingly, this all occurred in the face of activated pro-growth signaling pathways, including mTORC1, Myc, and PI3K/Akt. These observations highlight the evolutionarily conserved role of pyruvate metabolism in setting the balance between energy extraction and biomass production in specialized post-mitotic cells.

Introduction

Cells must appropriately allocate available nutrients to optimize their metabolic programs— for energy extraction and for the generation of building blocks that enable cell

growth. The balance between these processes not only maintains cellular health under varying nutritional conditions but also plays an important role in determining cell fate and function (Baker & Rutter, 2023; DeBerardinis & Thompson, 2012; Ghosh-Choudhary et al., 2020; Metallo & Vander Heiden, 2013). For example, hepatocyte metabolism changes considerably between fed and fasted conditions. In the fed state, hepatocytes use the majority of their nutrients to synthesize proteins, lipids, and glycogen, which results in increased cell size and liver biomass (Kast et al., 1988; Reinke & Asher, 2018; Sinturel et al., 2017). To meet the energy demands of other tissues during fasting, the liver undergoes a metabolic shift to produce glucose from biosynthetic precursors, thereby decreasing hepatocyte and liver size (Lang et al., 1998; Sinturel et al., 2017).

The metabolic pathways that support biosynthetic metabolism can be inappropriately activated in diseases such as cancer and heart failure to promote pathological growth. For example, many of the primary oncogenic adaptations in tumors prioritize anabolic metabolism over ATP production, which facilitates rapid cell proliferation (Lunt & Vander Heiden, 2011; Vander Heiden et al., 2009; Zhu & Thompson, 2019). Metabolic rewiring during heart failure similarly results in greater biosynthetic potential and less efficient ATP production, which in post-mitotic cardiomyocytes leads to increased cell size and insufficient cardiac pumping (Bornstein et al., 2024; Henry et al., 2024; Weiss et al., 2023).

The fate of pyruvate, which is primarily generated from glucose via glycolysis in the cytoplasm, is a critical node that can determine the balance between energetic and biosynthetic metabolism (Baker & Rutter, 2023; Yiew & Finck, 2022). In most differentiated cells, the majority of pyruvate is transported into the mitochondria via the mitochondrial pyruvate carrier (MPC) complex, a heterodimer composed of MPC1 and MPC2 proteins (Bricker et al., 2012; Herzig et al., 2012). Once in the mitochondria, pyruvate is converted to acetyl-CoA by the pyruvate dehydrogenase complex (PDH), fueling the tricarboxylic acid (TCA) cycle and supporting efficient ATP production. In cancer, stem, and other proliferative cells, more pyruvate is converted to lactate and exported from the cell, a process that regenerates NAD^+, a cofactor necessary for glycolytic flux (Baker & Rutter, 2023; Lunt & Vander Heiden, 2011; Zhu & Thompson, 2019). In some specialized cells, including hepatocytes, pyruvate is imported into mitochondria but converted to oxaloacetate, which can feed the TCA cycle but also serves as a precursor for glucose production via gluconeogenesis (Holecek, 2023b; Jitrapakdee et al., 2008). We and others have demonstrated that these alternative fates of pyruvate—energy generation, cell proliferation, or glucose production—differentially impact the metabolic and fate decisions of multiple cell types in varying contexts (Bensard et al., 2020; Cluntun et al., 2021;

Wei et al., 2022; Yiew & Finck, 2022). Loss of MPC function, which shifts pyruvate metabolism toward lactate production and thus expedites glycolysis and the production of biosynthetic precursors, has been shown to increase cell proliferation in mouse and *Drosophila* intestinal stem cells as well as in various tumors (Bensard et al., 2020; Schell et al., 2017; Zangari et al., 2020). MPC expression is also reduced in human and mouse models of heart failure, and genetic deletion of the MPC in cardiomyocytes is sufficient to induce hypertrophy and heart failure (Cluntun et al., 2021; Fernandez-Caggiano et al., 2020; McCommis et al., 2020; Zhang et al., 2020). Conversely, MPC overactivation or overexpression restricts intestinal stem cell proliferation and limits the growth of cardiomyocytes under hypertrophic stimuli, with excess mitochondrial pyruvate fueling the TCA cycle (Bensard et al., 2020; Schell et al., 2014; Schell et al., 2017). These observations suggest that mitochondrial pyruvate metabolism is central to cell proliferation as well as the size and specialized functions of post-mitotic cells.

The mechanisms regulating cell size include well-characterized cellular signaling pathways and transcriptional programs (Grewal, 2009; Liu et al., 2022; Lloyd, 2013). The CDK4-Rb pathway monitors cell size in proliferating cells by coupling cell growth with cell division (Amodeo & Skotheim, 2016; Ginzberg et al., 2018; Tan et al., 2021; Zhang et al., 2022). In response to insulin and other growth factors, the PI3K/Akt pathway activates mTORC1, leading to increased biosynthesis of proteins, lipids, and nucleotides, and consequently, increased cell size (Gonzalez & Hall, 2017; Gonzalez & Rallis, 2017; Saxton & Sabatini, 2017). The pro-growth transcription factor Myc drives a gene expression program that enhances metabolic activity and protein synthesis, resulting in larger cells (Baena et al., 2005; Dang, 1999; Iritani & Eisenman, 1999; Stine et al., 2015; van Riggelen et al., 2010). However, we only partially understand how metabolic pathways regulate physiological (or pathophysiological) growth, particularly in cells that have distinct and specialized roles in organismal metabolism.

Here, we investigated whether pyruvate metabolism influences biosynthetic capacity and cell size, using the *Drosophila* fat body as a model of the mammalian liver. We found that MPC overexpression and increased mitochondrial pyruvate transport restrict cell growth and limit protein synthesis in larval fat body cells and in spheroids of human liver-derived cells. Higher MPC expression resulted in smaller cells, not by increasing TCA cycle flux as observed in other cell types, but instead by redirecting mitochondrial pyruvate metabolism towards gluconeogenesis. A key driver of this metabolic rewiring is a reduced cellular redox state, which disrupts the biosynthesis of TCA cycle-derived amino acids, such as aspartate and glutamate, ultimately reducing protein synthesis. These observations highlight how cells with specialized

functions, like hepatocytes, employ distinct metabolic adaptations to respond to organismal demands under varying nutritional conditions.

Results

Increased mitochondrial pyruvate transport reduces the size of *Drosophila* fat body cells

The *Drosophila* fat body is functionally analogous to mammalian white adipose tissue and liver, serving as a buffer to store excess nutrients in fat droplets and glycogen and deploy them to support the animal with fuel during times of fasting (Arrese & Soulages, 2010; Musselman et al., 2013). During larval development, fat body cells halt cell division and dramatically increase in size during the third instar stage (from 72 to 120 hours After Egg Laying (AEL)) (Edgar & Orr-Weaver, 2001; Zheng et al., 2016) (Fig. 1a-c). As a first step toward understanding the metabolic programs that enable this rapid cell growth, we performed RNA sequencing of the *Drosophila* fat body across this developmental period. We observed a time-dependent change in mRNAs encoding proteins that have well-characterized roles in supporting cell growth, including components of the insulin and mTORC1 signaling pathways and the Myc transcriptional network which correlated with increased cell size (Supplementary Fig. 1a). Amongst metabolic genes, we observed modest differences in those that function in amino acid synthesis and fatty acid metabolism (Supplementary Fig. 1b). The abundances of mRNAs encoding proteins involved in glycolysis, oxidative phosphorylation (OxPhos), and the TCA cycle were distinctly altered in fat bodies during development (Supplementary Fig. 1b). Since pyruvate metabolism is the central node connecting carbohydrate metabolism and the TCA cycle, we studied the abundances of mRNAs that encode proteins that regulate pyruvate metabolism (Fig. 1d). We found that the expression of genes that link pyruvate to the TCA cycle were reduced including, *Pyk,* the *Drosophila* pyruvate kinase homolog, which converts phosphoenolpyruvate into pyruvate; *Mpc1* and *Mpc2,* which encode the two subunits of the MPC, which transports pyruvate into the mitochondrial matrix; as well as *Pdha* and *Dlat,* which encode subunits of PDH complex (Fig. 1e). In contrast, some mRNAs encoding proteins that regulate pyruvate abundance were upregulated such as *Pepck* and *Pepck2*, which make phosphoenolpyruvate from oxaloacetate (Supplementary Fig. 1c). Based on these data, we hypothesized that the suppression of mitochondrial pyruvate metabolism, which is gated by the action of the MPC, might support the rapid cell growth observed in fat body cells.

To test this hypothesis, we prevented the downregulation of the MPC during larval development (Fig. 1e) by ectopically expressing *Mpc1* and *Mpc2* (termed “MPC+” Supplementary Fig. 2a, 2b). The sustained expression of the MPC (both *Mpc1* and *Mpc2*)

throughout the fat body significantly reduced the rate of cell growth compared to a GFP-expressing control (Supplementary Fig. 2c). Given the important role of the fat body in controlling organismal growth, we wanted to assess the cell-autonomous effects of MPC expression using mosaic analysis in individual fat body cells (Supplementary Fig. 2d) (Ito et al., 1997). We generated GFP-labeled clones with expression of the MPC (MPC+), which we confirmed by immunofluorescence (Supplementary Fig. 2e, f). The MPC-expressing, GFP-positive cells were significantly smaller in size compared with either mock clones (control) or neighboring GFP-negative cells within the same tissue. *Mpc1* knock down (*Mpc1*-KD) clones, in contrast, were marginally larger (Fig. 1f-g). These results demonstrate that sustained expression of the MPC in developing fat body cells is sufficient to prevent cell growth in a cell-autonomous manner.

If the effects of MPC expression were related to the mitochondrial transport of pyruvate, then limiting the production of pyruvate should mitigate these effects. Therefore, we measured cell size in larvae raised on either a normal (9% sugar) diet or a diet with no added sugars, which limits the production of pyruvate from glucose and fructose. Limiting dietary sugars significantly reduced the size of control clones but increased the size of MPC-expressing clones. Notably, the size of MPC-expressing fat body clones was comparable to that of control clones when larvae were grown in sugar-limited medium, suggesting that limiting pyruvate synthesis abolishes the effect of MPC expression on fat body cell size (Fig. 1h, i). *Mpc1*-KD clones were again larger than control cells, and their size was unaffected by the sugar-limited diet. Inhibiting MPC activity by feeding larvae a normal diet supplemented with the MPC inhibitor UK5099 ameliorated the cell size effects of MPC expression (Fig. 1j; Supplementary Fig. 2g). These results indicate that pyruvate transport into mitochondria inversely correlates with the size gain in fat body cells. These observations also suggest that the suppression of mitochondrial pyruvate import and metabolism is required for the rapid cell size expansion observed in the fat body during larval development.

The size of a cell is determined by its content of proteins, nucleic acids, and lipids (Bjorklund, 2019; Lloyd, 2013; Schmoller & Skotheim, 2015). To understand how MPC expression affects the abundance of these macromolecules, we dissected fat bodies from control and fat body-wide MPC-expressing larvae at 120 hours AEL and quantified DNA, RNA, triacylgylcerides, and protein. Control and MPC+ fat bodies had equivalent DNA content (Fig. 1k; Supplementary Fig. 2h) and similar levels of EdU incorporation (Supplementary Fig 2o, p), suggesting that MPC expression does not impact DNA endoreplication. RNA and lipid content were modestly decreased in MPC+ fat bodies compared with control tissues (Fig. 1k;

Supplementary Fig. 2i, j), although the number of lipid droplets was higher with MPC expression (Supplementary Fig 2l-n). In contrast, MPC expression dramatically decreased protein abundance in fat bodies (Fig. 1k, Supplementary Fig. 2k), and reduced protein synthesis as assessed by staining for the puromycin analog, O-propargyl-puromycin (OPP) (Deliu et al., 2017; Villalobos-Cantor et al., 2023) (Fig. 1l, m). These data suggest that MPC-mediated mitochondrial pyruvate import decreases protein synthesis, which likely contributes to the reduced size of MPC-expressing cells. Conversely, in developing fly larvae, repression of the MPC and the subsequent decrease in mitochondrial pyruvate appear to provide a metabolic mechanism to support a rapid expansion in cell size.

Growth factor signaling pathways are hyperactivated in MPC expressing cells

The best understood mechanisms that govern cell size involve conserved signaling and transcriptional networks (Bjorklund, 2019; Grewal, 2009; Lang et al., 1998; Lloyd, 2013). For example, the mTORC1 pathway coordinates both extracellular and intracellular growth regulatory signals to dictate the synthesis and degradation of macromolecules, including proteins, lipids, and nucleic acids (Gonzalez & Hall, 2017; Gonzalez & Rallis, 2017; Saxton & Sabatini, 2017). mTORC1 increases protein synthesis through the phosphorylation of several proteins, including S6 kinase (S6K) and 4EBP1 (Fig. 2a). Since MPC-expressing clones were smaller in size and had reduced protein synthesis compared with control clones, we assessed mTORC1 activity in the fat body using our mosaic expression system. As a control, we confirmed that *S6k* (the *Drosophila* gene encoding S6K) over-expressing clones were larger in size and had elevated phospho-S6 staining compared with wild-type clones (Fig. 2b, c). Surprisingly, MPC+ clones also had elevated phospho-S6 staining (Fig. 2b, c), suggesting that despite their small size, these cells have high mTORC1 activity. Over-expression of *Rheb*, which is an upstream activator of mTORC1, resulted in clones that were larger than wild-type controls and which had increased phospho-4EBP1 staining (Fig. 2d, e). Again, even though the MPC+ clones were smaller in size, we observed robust p-4EBP1 staining, indicating that mTORC1 is hyperactive in these cells.

Gene set enrichment analysis of RNA-sequencing data from MPC-expressing fat bodies showed enrichment for signatures associated with pro-growth signaling (Supplementary Fig. 3a). We assessed markers of several of these pathways in MPC+ clones. In addition to the mTORC1 pathway, Myc increases cell growth by regulating the transcription of ribosome subunits and biosynthetic metabolic genes. We found that MPC+ clones had an elevated abundance of the Myc protein, both in the cytoplasm and nucleus, (Fig. 2f, g), suggesting that

the growth-promoting Myc transcriptional program is active in these cells. MPC+ clones also had reduced expression of the transcription factor Foxo, consistent with its downregulation by pro-growth signaling pathways (Supplementary Fig. 3b). Finally, we stained for phospho-eIF2α to assess the activity of the integrated stress response, which restricts global protein synthesis. Starvation robustly induced the integrated stress response in control clones, but MPC+ clones exhibited no evidence of activation of this pathway under normal growth conditions (Fig. 2h, i). Collectively these data indicate that conventional pro-growth pathways are activated in MPC-expressing clones, which is incongruent with the small size of the clones. This suggests that mitochondrial pyruvate metabolism controls cell size via alternative molecular mechanisms.

We next performed genetic epistasis analysis to better understand the relationship between MPC expression and the mTORC1, PI3K, and Myc pathways. Activation of the PI3K or mTORC1 pathways, via over-expression of *PI3K*, increased the size of control but not MPC-expressing fat body cells (Supplementary Fig. 3c). Similarly, activation of mTORC1 via knock down of its inhibitor, Tuberous Sclerosis Complex 1 (*Tsc1*), increased the size of control cells but had no effect on MPC+ cell size (Supplementary Fig. 3d). Over-expression of *Myc*, on the other hand, increased the size of control and MPC+ fat body clones to a similar degree (Supplementary Fig. 3e). Knock down of *Myc* was sufficient to decrease cell size to a similar extent as MPC expression; however, *Myc* knock down had no additional effect on cell size in MPC+ clones (Supplementary Fig. 3f). These results suggest that neither mTORC1, PI3K, nor Myc are epistatic to MPC and suggest that MPC likely acts independently of these canonical pathways to regulate the size of fat body cells.

Increased mitochondrial pyruvate transport reduces the size of HepG2 cells and spheroids

Since the *Drosophila* fat body has many features reminiscent of the mammalian liver, we tested whether MPC expression might similarly restrict cell size in cells derived from this tissue. We engineered HepG2 cells, which were originally isolated from a hepatocellular carcinoma, to express epitope tagged-MPC1 and MPC2 in a doxycycline-inducible manner. We observed expression of ectopic MPC1 and MPC2 starting at four hours after doxycycline treatment, which increased over the duration of the time course, peaking at 24 hours post-induction (Fig. 3a). We stained doxycycline-treated cells with phalloidin and measured cell size using microscopy images taken at two-hour intervals. Induction of MPC expression coincided with a significant reduction in cell size, which was first apparent six hours post-doxycycline treatment and was sustained for the remainder of the time course (Fig. 3b). Doxycycline had no effect on the size

of control HepG2 cells (EV). Treatment with the MPC inhibitor UK5099 for 24 hours markedly increased the size of control cells and partially reversed the small size phenotype of MPC-expressing cells (Fig. 3c). We also assessed cell volume by analyzing a 3D reconstruction of confocal images of phalloidin-stained HepG2 cells and found that the cell volume was lower in MPC+ cells (Supplementary Fig. 4a).

We have observed that the physiological consequences of altered pyruvate metabolism are more apparent in cells grown in a three-dimensional culture environment (Schell et al., 2014; Wei et al., 2022). Using our doxycycline-inducible cells, we found that MPC expression resulted in spheroids that were significantly smaller than control spheroids as assessed by microscopy (Fig. 3d, e). Cells from MPC-expressing spheroids were also smaller, as shown by flow cytometry (Fig. 3f, g). When compared with control (EV) spheroids, expression of MPC did not affect the number of cells per spheroid, the cell cycle phase distribution, or the number of apoptotic or necrotic cells (Supplementary Fig. 4b, 4c, and 4d). These analyses suggest that the smaller size observed in MPC expressing spheroids is not due to effects on cell proliferation or cell death.

Consistent with our observations in the *Drosophila* fat body, protein content was lower in MPC-expressing HepG2 spheroids compared with EV controls, whereas there was no difference in the abundances of DNA, RNA, or triacylglycerides (Fig. 3h; Supplementary Fig. 4e-h). To directly assess the effect of MPC expression on protein synthesis, we induced the MPC in HepG2 cells and treated the cells acutely with a low concentration of puromycin to label nascent proteins. We found that MPC expression decreased the incorporation of the amino acid analog L-homopropargylglycine (HPG) (Shen et al., 2021; Tom Dieck et al., 2012) into nascent proteins, as assessed by fluorescence microscopy (Fig. 3i, j). Protein synthesis was similarly reduced in MPC-expressing HepG2 spheroids (Fig. 3k, l). These observations were further supported by the decreased abundance of the short-lived, destabilized GFP (d2GFP) (Li et al., 1998; Pavlova et al., 2020) in MPC-expressing HepG2 spheroids compared with controls. This reduction in the level of d2GFP was prevented by treatment with the MPC inhibitor UK5099 (Fig. 3m). Together, these data suggest that increased transport of pyruvate into mitochondria, mediated by MPC expression, reduces protein synthesis and cell size in both fly and mammalian models.

Excess mitochondrial pyruvate promotes gluconeogenesis

We have previously shown that loss of the MPC reduces the contribution of glucose and pyruvate to the TCA cycle (Bensard et al., 2020; Cluntun et al., 2021). To investigate how MPC

expression impacts carbohydrate metabolism in HepG2 cells, we performed metabolic tracing using ^{13}C-glucose (Fig. 4a). We observed that MPC expression reduced the labeling fraction of the glycolytic intermediates 3-phosphoglycerate (Supplementary Fig. 5a) and pyruvate (Supplementary Fig. 5b), as well as alanine (Supplementary Fig. 5c), which is derived from pyruvate, all of which suggests a reduction in glycolysis in these cells. Once imported into mitochondria, glycolytic-derived pyruvate has two major fates: conversion to acetyl-CoA by PDH or to oxaloacetate by pyruvate carboxylase (PC). These fates can be differentiated by assessing the abundances of M+2 (derived from PDH) and M+3 (derived from PC) TCA cycle intermediates (Fig. 4a). We found that both M+2 and M+3 isotopomers of TCA cycle intermediates were modestly increased following MPC expression (Fig. 4b and 4c; Supplementary Fig. 5d-i). The fact that we observe increases in TCA cycle intermediates despite decreased glycolytic labeling in pyruvate suggests that the apparent labeling through PDH and PC might be underestimating the effect on metabolic flux through these enzymes. Thus, it appears that MPC expression increases the activity of both enzymes that utilize pyruvate. Typically, when TCA cycle flux is increased, one observes an increase in activity of the electron transport chain (ETC) to oxidize the resulting NADH. However, MPC expression had no impact on ETC activity as assessed by measuring oxygen consumption (Fig. 4d). The implications of elevated NADH production without a concomitant increase in NADH oxidation will be discussed in Fig. 5.

To probe the impact of increased flux through the PC and PDH reactions, we conducted genetic epistatic analysis in fat body cells. We found that *Drosophila* fat body clones in which we over-expressed *Pcb* (the *Drosophila* gene encoding pyruvate carboxylase) were significantly smaller than controls and were equivalent in size to MPC+ clones (Fig. 4e, f; Supplementary Fig. 6a-c). Clones expressing both the MPC and *Pcb* were even smaller (Fig. 4e, f; Supplementary Fig. 6a-c). Conversely, knockdown of *Pcb* (*Pcb*-KD) in MPC-expressing fat body clones completely rescued the cell size phenotype (Fig. 4e, f; Supplementary Fig. 6d). Knockdown of *Pcb* in MPC-expressing HepG2 cells also eliminated the small cell size phenotype (Supplementary Fig. 6e). These data suggested that the small size of cells expressing the MPC is likely due to increased flux through the PC reaction. Consistent with this, knock down of the PDH-E1 (*Drosophila* gene *Pdha*) or PDH-E2 (*Drosophila* gene *Dlat*) subunits of PDH, which should divert mitochondrial pyruvate, so it is preferentially used by PC, also resulted in smaller fat body cells (Supplementary Fig. 6f-k). In contrast, activating PDH by knocking down the inhibitory PDH kinases (mammalian PDKs, *Drosophila* gene *Pdk*) (Stacpoole, 2017; Wang et al., 2021), which should promote the flux of pyruvate through PDH

and away from PC, rescued cell size in MPC-expressing fat body clones (Supplementary Fig. 6j, k). Similarly, in MPC-expressing HepG2 cells, activation of PDH via treatment with the PDK inhibitors DCA and AZD7545 was sufficient to restore cell size (Supplementary Fig. 6l), (Stacpoole, 2017; Wang et al., 2021). These analyses suggest that the reduction in cell size observed with MPC expression is due to PC-mediated metabolism of pyruvate.

The product of PC, oxaloacetate, has three major metabolic fates: 1) feeding the TCA cycle via citrate synthase as discussed above, 2) conversion to aspartate by glutamic-oxaloacetic transaminase 2 (GOT2), and 3) conversion to phosphoenolpyruvate by PEPCK2, leading to gluconeogenesis, synthesis of glucose (Jitrapakdee et al., 2008; Kiesel et al., 2021). Sustained expression of the MPC in fat bodies increased the concentration of glucose in this tissue (Fig. 4g) as well as glucose and trehalose in larval circulation (known as hemolymph) (Fig. 4h), suggesting that MPC expression increases glucose production in fat body cells. Next, we tested whether PEPCK2-mediated gluconeogenesis was elevated in these cells compared with controls. We used ^{13}C-lactate to trace the ^{13}C-labeling of phosphoenolpyruvate and resultant glucose synthesis via gluconeogenesis (Fig. 4i). We found that the relative abundance of M+3 phosphoenolpyruvate was higher in MPC-expressing cells compared with controls (Fig. 4j), suggesting increased activity of PEPCK2. The gluconeogenic pathway employs a series of biochemical reactions to convert phosphoenolpyruvate into glucose, which is then excreted from the cell. This production of M+6 glucose from lactate was also higher in MPC-expressing HepG2 cells (Fig. 4k). To test whether gluconeogenesis contributes to the small size phenotype of MPC-expressing cells, we knocked down enzymes in the pathway (*Drosophila* phosphoenol carboxykinase, *Pepck2,* and fructose bisphosphatase, *Fbp*) and assessed cell size in *Drosophila* and HepG2 models. Knockout of PEPCK2 rescued the size of MPC-expressing HepG2 cells grown in spheroids (Fig. 4l) and cells (Supplementary Fig. 6m). Knockdown of either *Pepck2* or *Fbp* partially rescued the size defect in MPC-expressing *Drosophila* fat body clones (Fig. 4n, o; Supplementary Fig. 6n-r), and *Pepck2* knockdown also increased protein synthesis in these clones (Fig. 4p, q). Collectively, these data suggest that the cell size and protein synthesis phenotypes observed in MPC-expressing cells require PC-mediated gluconeogenesis, and this relationship is found in both the *Drosophila* fat body and in HepG2 cells.

A redox imbalance impairs protein synthesis and cell growth in MPC-expressing cells

We were intrigued by the observation that MPC expression exerted its impact on cell size through PC, rather than via increased flux through PDH. We did not observe any

differences in the abundances of PDH1a, phosphorylated (Ser-293, inactive) PDH1a, PC, PEPCK2, or G6PC proteins in MPC-expressing HepG2 cells (Supplementary Fig. 7a, b). We therefore hypothesized that the shift in pyruvate metabolism in response to MPC expression might be driven by changes in the abundances of enzyme cofactors, metabolite regulators, or cellular redox balance. PC and PDH show reciprocal regulation by such factors: PC utilizes ATP as a substrate and is allosterically activated by acetyl-CoA, whereas PDH is inhibited by ATP, acetyl CoA, and NADH (Chai et al., 2022; Sugden & Holness, 2011) (Supplementary Fig. 7c). In addition, several reactions in gluconeogenesis require ATP or NADH (Hausler et al., 2006; Siess et al., 1977) (Supplementary Fig. 7c). Upon induction of MPC expression in HepG2 cells, we observed increased abundance of acetyl-CoA (Supplementary Fig. 7d), a higher ATP to ADP ratio (Supplementary Fig. 7e), a greater abundance of NADH without an increase in NAD^+, and thus an increase in the cellular NADH/NAD^+ ratio (Supplementary Fig. 7f-h). To determine how MPC expression impacts the subcellular distribution of redox factors, we separated cytoplasmic and mitochondrial fractions from control or MPC-expressing *Drosophila* fat bodies and measured the NADH/NAD^+ ratio. We found that MPC expression increased the NADH/NAD^+ ratio in both the cytoplasm and mitochondria (Fig. 5a). We observed a similar increase in the NADH/ NAD^+ ratio in both fractions in MPC-expressing HepG2 spheroids (Fig. 5b). It is important to note that these measurements can be confounded by the very rapid redox reactions that can happen post-harvest. Nonetheless, these combined results suggest that the increased abundances of acetyl-CoA, ATP, and NADH in MPC-expressing cells could promote the rewiring of mitochondrial pyruvate metabolism through PC and support gluconeogenesis.

To test the hypothesis that ATP or NADH concentrations might affect cell size in MPC-expressing *Drosophila* fat body clones or HepG2 cells, we utilized pharmacological or genetic modulation of these molecules. Treatment with gramicidin, which decreases the ATP to ADP ratio (Xue et al., 2022), did not alter the size of MPC-expressing HepG2 cells (Supplementary Fig. 7i). We used several orthogonal approaches to reduce the cellular NADH/NAD^+ ratio in the MPC-expressing systems and measured their effect on cell size. Co-expression of the *Drosophila* nicotinamide mononucleotide adenylyl transferase (*Nmnat)*, which increases NAD^+ biosynthesis, almost normalized the small size phenotype of MPC-expressing clones in the *Drosophila* fat body (Fig. 5c, d). We observed a similar rescue of cell size following expression of the *Ciona intestinalis* alternate Complex I enzyme NADH dehydrogenase (NDX) (Gospodaryov et al., 2020) or the yeast NADH dehydrogenase (NDI) (Sanz et al., 2010), both of which oxidize NADH to NAD^+ without concomitant proton translocation and energy capture (Fig. 5e, f). Expression of NDI in HepG2 cells also mitigated the effect of MPC expression on

spheroid size (Supplementary Fig. 7j, k), as did treatment with duroquinone (Merker et al., 2006) (Supplementary Fig. 7l), which oxidizes NADH to NAD^+. To extend these investigations to three-dimensional culture, we supplemented the growth medium of MPC-expressing HepG2 spheroids with the NAD^+ precursors nicotinamide riboside (NR) or nicotinamide mononucleotide (NMN), both of which recovered spheroid size (Fig. 5g, h).

Since MPC expression reduced protein synthesis in both *Drosophila* fat bodies and HepG2 cells, we tested how cellular redox status might contribute to this phenotype in both systems. Expression of NDX, which lowers the NADH/NAD^+ ratio, increased translation in MPC-expressing *Drosophila* fat body clones (Fig. 5i, j). In HepG2 spheroids, boosting NAD^+ biosynthesis by supplementing growth media with NR or NMN partially rescued the abundance of destabilized GFP (Fig. 5k). These results suggest that the elevated NADH/ NAD^+ ratio in MPC-expressing cells limits protein synthesis and that normalizing that ratio increases protein synthesis and cell size.

Reduced amino acid abundance impairs the size of MPC-expressing cells

Given the reduced protein synthesis observed upon MPC expression, we assessed amino acid concentrations in HepG2 using steady-state metabolomics. We found that MPC expression reduced the abundance of most amino acids (Fig. 6a). To test whether the low abundances of amino acids contribute to the smaller size of MPC-expressing cells, we supplemented the growth media of HepG2 spheroids with excess non-essential amino acids (NEAAs)—either two or three times the recommended dilution of a commercially available amino acid cocktail that includes glycine, L-alanine, L-asparagine, L-aspartate, L-glutamate, L-proline, and L-serine. MPC-expressing spheroids grown with excess NEAAs were comparable in size to controls (Fig. 6b, c). In parallel, we provided *Drosophila* larvae with food containing excess (5x) amino acids from 72 to 120 hours AEL, which partially rescued cell size in MPC-expressing fat body clones (Fig. 6d, e). To genetically augment intracellular amino acids, we expressed the amino acid importer *slimfast* (Colombani et al., 2003) in control or MPC-expressing fat body clones and found that it prevented the decrease in cell size (Fig. 6f, g).

To determine which amino acid(s) contribute to the cell size effects of MPC expression, we cultured control and MPC-expressing HepG2 cells in media supplemented with an excess of each amino acid from the NEAA cocktail. Treatment with excess glycine, L-alanine, or L-serine had no effect on cell size (Fig. 6h). However, the size of MPC-expressing cells was normalized by supplementation with L-aspartate, L-glutamate, or L-proline (Fig. 6h), all of which are derived from TCA cycle intermediates. Supplementation with either L-aspartate or L-glutamate also

rescued the small size phenotype of MPC-expressing HepG2 spheroids (Supplementary Fig. 8a, b). Increasing L-aspartate uptake by over-expressing the aspartate transporter SLC1A3 also recovered size of HepG2 spheroids (Supplementary Fig. 8c, d). In addition, treatment with excess (3x) NEAA partially restored the abundance of d2GFP in MPC-expressing HepG2 spheroids (Supplementary Fig. 8e), suggesting rescued protein synthesis.

Like glutamate and proline, aspartate is derived from a TCA cycle intermediate, specifically via transamination of oxaloacetate by glutamic-oxaloacetate transaminase 2 (GOT2). Since GOT2 and PEPCK2 both utilize oxaloacetate as a substrate, we hypothesized that knocking down GOT2 might phenocopy MPC expression by driving PEPCK2-mediated conversion of oxaloacetate into phosphoenolpyruvate and thereby suppressing aspartate biosynthesis. Knock down of *Got2* (the *Drosophila* gene encoding GOT2) reduced cell size in *Drosophila* fat body clones and phenocopied MPC-expressing cells (Fig. 6i, j; Supplementary Fig. 8f-h). Similarly, both GOT2 knock out and MPC-expressing HepG2 cells were smaller than EV (Supplementary Fig. 8i). Expression of the MPC in these GOT2 knock down systems had no significant impact on cell size (Fig. 6i, j; Supplementary Fig. 8i), suggesting that the effects of MPC expression and GOT2 knock down act similarly to limit amino acid synthesis and cell size. We next performed the reciprocal experiment by over-expressing *Got2* to favor the production of aspartate from oxaloacetate. *Got2* expression normalized cell size in both MPC-expressing fat body clones and in HepG2 spheroids (Fig. 6i, j; Supplementary Fig. 8j, k). The efflux of aspartate from mitochondria into the cytoplasm is a critical component of the malate-aspartate shuttle, which is a major redox shuttle in human cells. To test whether increasing the abundance of aspartate would ameliorate the high $NADH/NAD^+$ ratio observed in MPC-expressing cells, we supplemented growth media with exogenous aspartate and assessed cellular redox status. We found that excess aspartate reduced the cellular $NADH/NAD^+$ ratio in these cells such that it was comparable with control cells (Fig. 6k). We observed similar results when we treated these cells with NMN or UK5099 (Fig. 6k). Moreover, all these treatments increased protein synthesis in MPC-expressing cells (Fig. 6l, m).

Mitochondrial pyruvate import reduces the size of rat primary hepatocytes

Although HepG2 cells exhibit some features of hepatocytes, they are a transformed, immortalized, and proliferative hepatocellular carcinoma cell line. We wanted to test whether the MPC expression phenotypes that we observed in *Drosophila* fat bodies and HepG2 cells could be recapitulated in a more physiologically relevant mammalian model. We chose primary rat hepatocytes, which have been used extensively to interrogate hepatocyte cell metabolism and

signaling and also have the advantage of being genetically tractable. We expressed MPC1 and MPC2 in cultured primary rat hepatocytes (Fig. 7a), and, consistent with our results in other systems, we found that expression of MPC reduced cell size (Fig. 7b, c) and decreased protein synthesis (Fig. 7d). MPC-expressing primary hepatocytes also had a higher NADH to NAD^+ ratio in both the cytoplasmic and mitochondrial fractions (Fig. 7e). We assessed gluconeogenesis in primary hepatocytes by quantifying glucose in the culture media following incubation with the gluconeogenic precursors, pyruvate, and lactate. Glucose production was higher in MPC-expressing hepatocytes compared with controls (Fig. 7f). Treatment with UK5099 eliminated this effect and reduced glucose production to a similar rate in both cells (Fig. 7f). These results demonstrate that augmented mitochondrial pyruvate in hepatocytes, and related cells in *Drosophila*, drives a metabolic program that results in an increased NADH/NAD^+ ratio. This scenario results in accelerated gluconeogenesis, decreased protein synthesis, and reduced cell size.

Discussion

We investigated whether pyruvate metabolism influences biosynthetic capacity and cell size in the *Drosophila* fat body and in HepG2 spheroids. During the third instar phase of *Drosophila* larval growth, when cells are rapidly expanding in size, we observed a profoundly decreased expression of the MPC in liver-like fat body cells. We found that this rewiring of pyruvate metabolism is essential for cell growth as forced maintenance of MPC expression resulted in dramatically smaller cells. By combining *Drosophila* genetic analyses and metabolomics studies in HepG2 cells and spheroids, we demonstrated that excess mitochondrial pyruvate elevates the cellular NADH/NAD^+ ratio and redirects carbohydrate metabolism to favor gluconeogenesis over glycolysis (Fig. 7g). This shift reduces the availability of oxaloacetate for aspartate and glutamate biosynthesis, triggering a broader imbalance in amino acid abundances within the cell. We conclude that altering the fate of pyruvate to support biomass accumulation is required for the cell size expansion that occurs during fat body development. We speculate that this phenomenon also applies to the mammalian liver, which is the closest analog of the *Drosophila* fat body, as both HepG2 cells and primary rat hepatocytes show similar effects following ectopic MPC expression.

Why does simply reorienting the metabolism of pyruvate have this profound effect on cell growth? Our data suggest that a central mediator of the phenotype is an elevated NADH/NAD^+ ratio, which likely results from MPC expression driving an acceleration of the TCA cycle, as evidenced by an increase in the abundances of M+2 isotopomers of TCA cycle intermediates.

Although the increase in labeled succinate, fumarate, and malate is modest, it occurs despite a reduction in glycolytic labeling. This suggests that less labeled pyruvate feeds the TCA in MPC-expressing cells compared with controls and that we are likely underestimating the actual increase in flux. The TCA cycle generates NADH and appears to do so more actively in cells with ectopically expressed MPC. However, our oxygen consumption data suggest that the oxidative phosphorylation system in these cells does not have the capacity to increase its activity in response to the enhanced availability of mitochondrial pyruvate and an increased $NADH/NAD^+$ ratio. As a result, the increased TCA cycle flux and limited ETC activity together elevate the $NADH/NAD^+$ ratio in both the mitochondria and cytoplasm, disrupting cellular redox balance leading to a rewiring of cellular metabolism.

This redox situation causes two distinct but related perturbations that appear to both contribute to decreased cell growth. First, we observed a clear depletion of amino acids and evidence of decreased synthesis of amino acids that are primarily derived from TCA cycle intermediates (aspartate, glutamate, and proline). A reduced NAD^+ pool impairs the capacity of cells to synthesize aspartate (Birsoy et al., 2015; Sullivan et al., 2015; Sullivan et al., 2018), which is used to synthesize glutamate and proline and which plays a crucial role in maintaining redox balance in both the mitochondria and cytoplasm (Alkan et al., 2018; Holecek, 2023a; Lieu et al., 2020; Wei et al., 2020; Yoo et al., 2020). Replenishing any of these TCA cycle-derived amino acids via genetic or nutritional increases in their availability was sufficient to reverse the effect of ectopic MPC expression on cell size. Thus, amino acid depletion is a key driver of the small size phenotype. Second, the increased $NADH/NAD^+$ ratio also drives a particular metabolic program that favors the conversion of mitochondrial pyruvate to oxaloacetate and a subsequent increase in gluconeogenesis. This program is enforced by allosteric regulation via NADH, acetyl-CoA, and ATP, which act on PC and several enzymes of glycolysis and gluconeogenesis. It also appears to be important for the small size of MPC-expressing cells since loss of any of several steps along the gluconeogenic pathway, particularly PC and PEPCK2, mitigates or eliminates the cell size phenotype observed with ectopic MPC expression in fat body cells and HepG2 spheroids. It is important to note that gluconeogenesis is a critical function of these cells, and its rate is carefully controlled in response to varying physiological stimuli. Surprisingly, constitutive MPC expression is sufficient to supersede the control enacted by physiological and hormonal signals and enact the loss of biomass and impaired cell size.

We have previously shown that loss of the MPC enhanced the stem cell identity and proliferation of intestinal stem cells, whereas ectopic MPC expression had the opposite effect (Bensard et al., 2020; Schell et al., 2017). Such observations are consistent with our findings

that MPC expression inversely correlates with biomass accumulation. More recent data demonstrated that enhanced MPC activity prevented the increase in cell size that occurs in cardiomyocytes in response to hypertrophic signaling (Cluntun et al., 2021; Fernandez-Caggiano et al., 2020). In these cases, the fate of mitochondrial pyruvate that determines cell growth is its oxidation in the TCA cycle. In contrast, our studies of hepatocytes and related cells described herein, demonstrate that the fate of pyruvate that suppresses growth in cell size is not oxidation by the TCA cycle, but rather the production of glucose, which starts with its conversion to oxaloacetate by PC in the mitochondria. Cardiomyocytes have low expression of PC compared with liver, where this enzyme (as well as others including PEPCK2) serves a vital role during fasting by producing glucose, which fuels the brain and other organs that require glucose for their survival and function (Hatting et al., 2018; Petersen et al., 2017; Rui, 2014). This is an example of how the unique metabolic physiology of specialized cells plays a critical role in maintaining organismal homeostasis.

One conclusion from the data presented herein is that a cell's metabolic program plays a decisive role in determining the growth of that cell. It was striking how rapidly expression of the MPC impacted cell size in the HepG2 model. Essentially, as soon as MPC over-expression became detectable, the population of cells started to show a decrease in size. Notably, the decrease in cell size following ectopic MPC expression occurred despite the upregulation of multiple pro-growth signaling networks. It is unclear why these networks are hyperactivated in this context as there is no evidence from our data indicating any nutrients are in excess abundance. We hypothesize that there may be regulators of cell size that recognize when cells are inappropriately small and engage these pathways to increase cell size. mTORC1, PI3K, and Myc pathways typically promote biomass accumulation and increased cell size but fail to do so when mitochondrial pyruvate is elevated. MPC expression reduced the abundance of amino acids, and this appears to play a dominant role to impair protein synthesis and prevent the cell growth effects expected following hyperactivation of the mTORC1 and Myc pathways. Thus, our data suggest that the metabolic fate of pyruvate can override canonical pathways that mediate cell size—such as mTORC1 signaling.

We demonstrate that the appropriate partitioning of pyruvate metabolism maintains the redox state of a cell to support the accumulation of biomass that is necessary for its specialized function. Increased mitochondrial pyruvate metabolism in cells from the fly "liver-like" fat body disrupts these processes, causes cells to perform excess gluconeogenesis, and prevents cell growth. As a result, the *Drosophila* larvae became hyperglycemic and experience developmental delay. The abundances of MPC1 and MPC2 are upregulated in mouse livers

during starvation and in high-fat diet conditions, which correlates with increased rates of gluconeogenesis in both circumstances. Conversely, loss of the MPC in the liver impairs gluconeogenesis (Gray et al., 2015; McCommis et al., 2015; Yiew & Finck, 2022). Moreover, liver dysfunction in diabetes and hepatic steatosis are driven by reductive stress and an elevated $NADH/NAD^+$ ratio (Goodman et al., 2020; Jokinen & Luukkonen, 2024). We are intrigued by the possibility that the fate of pyruvate might have profound consequences on the redox state and gluconeogenic capacity of the mammalian liver, including by functioning as part of the metabolic milieu that drives unrestrained gluconeogenesis in diabetes. Our discovery that mitochondrial pyruvate regulates the cellular redox state, thereby controlling biosynthesis, offers insights for developing therapeutic strategies for these and other diseases.

Methods

Drosophila Strains and Handling

Drosophila melanogaster stocks were maintained at 25°C on semi-defined fly food composed of 20 g agar, 80 g baker's yeast, 30 g sucrose, 60 g glucose, 0.5 g MgSO4, 0.5 g CaCl2, 11 ml tegosept, and 6 ml propionic acid. This was base medium for all *Drosophila* experiments, but specific fly food modifications are mentioned in text and figure legends. To induce clones in fat bodies, synchronized eggs were transferred to 29°C for 4 days until dissection. For experiments involving genetic manipulation of all fat body cells, *tubGal80^{ts20}* was used to restrict activity of *CG-Gal4* at 18°C for 120 hours (57 hours equivalent time at 25°C) and larvae were shifted to 29°C till dissection at specified time points.

Following fly stocks were procured from Bloomington stock center *UAS-MPC1-P2A-MPC2* (28812582)*, CG-Gal4; tubGal80^{ts20}, hs-Flp1.22 (*BDSC, #77928), *Act>CD2>Gal4, UAS-GFP* (BDSC, #4413), *Act>CD2>Gal4, UAS-RFP* (BDSC, #30558), *UAS-S6K^{STDETE}* (BDSC, #6914), *UAS-Rheb^{PA}* (BDSC, #9689), *UAS-Myc^{OE}* (BDSC, #9675), *UAS-Myc^{RNAi}* (BDSC, #25783), *UAS-PI3K93E$^{.ExcelI}$* (BDSC, #8287), *UAS-PI3K93E^{A2860C}* (BDSC, #8288), *UAS-TSC1^{RNAi}* (BDSC, #31314), *UAS-hPC* (BDSC, #77928), *UAS-PC^{RNAi}* (BDSC, #56883), *UAS-PEPCK2^{RNAi}* (BDSC, #36915), *UAS-FBPase^{RNAi}* (BDSC, #51871), *UAS-Pdk^{RNAi}* (BDSC, #35142), *UAS-NMNAT* (BDSC, #37002), *UAS-CintNDX* (BDSC, #93883), *UAS-ScerNDI1* (BDSC, #93878), *UAS-Slif* (BDSC, #52661), *UAS-GOT2^{RNAi}* (BDSC, #78778). From VDRC *UAS-MPC1$^{RNAi(KK)}$ and from NIG UAS-Pdha^{RNAi}, UAS-Dlat^{RNAi} (PDH E2)* were purchased.

Generation of Overexpression and CRISPR Mutant fly stock

Pc and *Pepck2* deletion fly stocks were generated using CRISPR-Cas9 as described (Gratz et al., 2014). We targeted specific nucleotide sequences of the genes of interest through homology-directed recombination using two guide RNAs and inserted a dsRed construct that expresses in adult eyes to facilitate the selection of mutant flies. We deleted exon 1 to exon 5 using guide RNAs for *Pc⁻KO*: 5′ guide ATACATTTAAGTCCTAGGC; 3′ guide TCGATTGATCCTGGAAACA. *Pepck2⁻KO*, being a single exon coding sequence, we generated complete deletion by using guides 5′ guide AAAGGGTGCACATCTGTGA; 3′ guide TTTGGGGCGTGGCCTAGAC. The plasmids were injected into y[1] M{GFP[E.3xP3]=vas-Cas9.RFP}ZH-2A w[1118] (BDSC, #55821) fly stock embryos (Bestgene) and one *Pc-KO* and five *Pepck2-KO* flies were picked up, confirmed for the dsRed expression in adult eyes and used in subsequent experiments.

To overexpress *Got2*, *Got2* cDNA was amplified from RNA extracted from larval fat bodies using primer 5' GAATTC ATGAGTAGAACCATTATTATGACGCTTAAGGAC, 3' CTCGAG CTTGGTAACCTTGTGTATGCTCTCAGCCAGG. The cDNA was then cloned into a pUAST-aatB plasmid using EcoRI and XhoI restriction enzymes, and the construct was injected into pBac{yellow[+]-attp-9A}VK00005 (BDSC, #9725) embryos to obtain the insertion

Mosaic Analysis and Phalloidin Staining for Cell Size Analysis

Fat body clones were induced by the leaky expression of heat shock flippase 1.22 during embryonic stages, and the 2D size of fat body cells was analyzed at 120 hours after egg laying (AEL) using fluorescence microscopy. Cell size analysis was conducted as reported earlier (Toshniwal et al., 2019). Fat bodies were dissected from larvae at the specified time points in 1X PBS buffer (pH 7.2, Invitrogen, #10010049) and fixed in 8% paraformaldehyde (Sigma Aldrich, # P6148) for 1 hour at room temperature (RT). The tissues were then washed twice with 0.1% PBT (0.1% Triton X-100 (Sigma Aldrich, # X100) in 1X PBS buffer) for 10 minutes each. Subsequently, the tissues were incubated with Rhodamine Phalloidin (Thermo Scientific, # R418) at a 1:400 dilution in 1X PBS buffer for 2 hours at room temperature (RT). After staining, the tissues were washed once with 0.1% PBT and then with 1X PBS before being mounted in DAPI-supplemented VectaShield (Vector Labs, #H1200). Representative images were captured using a Laser Scanning Confocal Microscope (LSM 880, Carl Zeiss). For cell size analysis, images were captured with a fluorescence microscope (Carl Zeiss, Axio Vision) at 20X magnification, focusing on a plane where all nuclei were in focus. The 2D areas of fat body cells were measured using FIJI software. Cell membranes stained with Rhodamine Phalloidin were traced using the freehand tool, and the area of approximately 20-25 GFP-positive cells from fat

bodies collected from about five animals was measured as one replicate. All cell size analyses were conducted in a blinded manner.

Immunofluorescence on Fat Body Clones

Larval fat bodies at 120 hours after egg laying (AEL) at 29°C were dissected in 1X PBS buffer (pH 7.2), fixed in 8% paraformaldehyde for 1 hour at room temperature (RT), and then washed three times in 0.1% PBT (0.1% Triton X-100 in 1X PBS buffer) for 10 minutes each. The tissues were blocked in 10% normal goat serum (NGS, Jackson ImmunoResearch Laboratories, #005-000-121) in 0.1% PBT for 1 hour at RT, followed by incubation with primary antibodies overnight at 4°C. Secondary antibody incubation was performed for 2 hours at RT. Following three to four washes in 0.3% PBT (10 minutes each) at RT, the tissues were mounted in DAPI-supplemented Vectashield (Vector Laboratories, #H1200). Images were captured using a Laser Scanning Confocal Microscope (LSM 880, Carl Zeiss).

Image Acquisition and Analysis

For all experiments, confocal images were captured using the same laser power and identical settings, with z-stacks of the dissected tissue taken at 1 μm intervals along the Y-axis. The images were analyzed using Fiji software, where a similar number of z-stacks focusing on the nuclei were projected at mean intensities. Using the freehand tool, cell membranes were outlined, and the mean fluorescence intensity (mean gray value) for each cell was recorded. To account for background fluorescence, the average mean gray values of the background (measured from regions of interest [ROI] of the same size) were subtracted from the recorded mean gray values of the cells. The resulting mean gray values, adjusted for background fluorescence, were then normalized, and the percent normalized mean gray values (with standard deviation, SD) of GFP-negative and GFP-positive cells were plotted.

Measurement of Protein Synthesis in Fat Bodies

Protein synthesis in *Drosophila* fat bodies was analyzed using the Click-iT Plus OPP Alexa Fluor 594 kit (Molecular Probes, #C10457). Fat bodies were dissected at 120 hours AEL in Shields and Sang M3 Insect Media (SSM3, Sigma, #S8398) and incubated with 5 mM O-propargyl-puromycin (OPP) in SSM3 media for 30 minutes at RT. Tissues were then washed three times with 1X PBS for 10 minutes each and fixed in 8% paraformaldehyde for 1 hour at RT. After fixation, the tissues were washed twice with 0.1% PBT (0.1% Triton X-100 in 1X PBS) supplemented with 0.5% bovine serum albumin (BSA) for 10 minutes each. The OPP was developed for 30 minutes at RT using the Click-iT reaction mixture, which included 88 μl of OPP Reaction Buffer, 20 μl of Copper (III) Sulfate (component D), 2.5 μl of component B, and 100 μl

of Buffer Additive (component E), following the manufacturer's instructions. The tissues were then washed twice in Reaction Rinse Buffer for 10 minutes each, followed by two washes in 0.1% PBT supplemented with 0.5% BSA for 10 minutes each at RT. After a final wash in 1X PBS, the fat bodies were mounted in DAPI-supplemented Vectashield. Images were captured using a confocal microscope (LSM 880, Zeiss).

LipidTOX Staining in Larval Fat Body Tissues

At 120 hours AEL, 3rd instar larvae were dissected in 1X PBS. The fat bodies were fixed in 8% paraformaldehyde for 1 hour at room temperature. After fixation, tissues were rinsed twice with 1X PBS. They were then incubated for 30 minutes in a 1:100 dilution of LipidTOX Red (Invitrogen, #H34351) in PBS, followed by two additional rinses with PBS. The tissues were mounted in DAPI-supplemented Vectashield and imaged using a confocal microscope. To quantify lipid droplet size, the diameters of lipid droplets from 35 fat body clones were measured using FIJI software.

EdU Incorporation in Fat Bodies

At 120 hours AEL, fat bodies were dissected in 1X PBS and incubated with 5 μM 5-ethyl-2'-deoxyuridine (EdU) in 1X PBS for 30 minutes at room temperature. The tissues were then washed three times with 1X PBS for 10 minutes each, followed by fixation in 8% paraformaldehyde for 1 hour at room temperature. After fixation, the tissues were washed with 0.1% PBT supplemented with 0.5% bovine serum albumin. EdU detection was performed using Click-iT Plus EdU Alexa Fluor 594 (Molecular Probes, #C10639) for 30 minutes at room temperature, according to the manufacturer's instructions. Following development, the fat bodies were mounted in DAPI-supplemented Vectashield. Images were captured using a confocal microscope (LSM 880, Zeiss).

RNA Isolation and RNA Sequencing

To collect fat body tissues, w^{1118} flies were mated at 25°C. The following day, flies were starved for one hour, and eggs were collected every 2 hours. The first collection was discarded, and the subsequent two collections were incubated at 25°C. After 20 hours, early hatched 1st instar larvae were discarded, and 1st instar larvae collected over a 2-hour period were kept at 25°C. Fat bodies from 10 male larvae at the specified time points were dissected and preserved in 1X PBS. For RNA isolation from MPC-overexpressing fat bodies at 120 hours AEL, RNA was extracted and purified using the NucleoSpin RNA kit (Takara Bio USA, Inc., #740955.50) with on-column DNA digestion, as per the manufacturer's instructions. Four independent samples for each time point were prepared for sequencing.

Library preparation for poly(A)-selected RNAs was carried out using the Illumina RNA TruSeq Stranded mRNA Library Prep Kit with oligo-dT selection. Sequencing was performed using the Illumina NovaSeq Reagent Kit v1.5 (150 bp paired-end reads) at the High-Throughput Genomics Core Facility at the University of Utah. The raw sequencing data were analyzed using the BDGP6.28 genome and gene feature files. Differentially expressed genes were identified using DESeq2 version 1.30.0 with a 5% false discovery rate. RNA quality control, library preparation, and sequencing were performed by the University of Utah Huntsman Cancer Institute High Throughput Genomics and Bioinformatics Shared Resource. RNA-seq data from this study are available at NCBI GEO.

QPCR

500 ng RNA was used to make cDNA using Superscript II reverse transcriptase (Molecular Probes, #18064-022), dNTP (Molecular Probes, #18427-088) and oligodT (Molecular Probes, #18418012). QPCR analyses were performed on cDNA as described using PowerUp SYBR Green Master Mix (Applied Biosystems, #2828831) on QuantStudio 7 Flex (Applied Biosystems) instrument. Fold changes in transcript level were determined using the ΔΔCt method. Transcript levels were normalized to *rp49*. Each experiment was performed using 4–5 independent samples. Following primers were used to do qPCR. List of primers is provided in Appendix 3

Hemolymph Glucose and fat body glucose measurement

Glucose concentrations in larval hemolymph and fat bodies were measured as previously described (Ugrankar-Banerjee et al., 2023). To isolate hemolymph, 10 third instar larvae were selected from culture tubes, thoroughly washed to remove any food residues, and then dried. Hemolymph was collected by bleeding the larvae on a parafilm strip using Dumont 5 forceps (Fine Science Tools, #11254-20). Two microliters of the colorless hemolymph were transferred to a 96-well plate and mixed with 200 µl of Autokit Glucose reagent (Wako, #997-03001). For measuring intercellular glucose, fat bodies were dissected from 10 larvae per genotype and homogenized in approximately 300 microliters of ice-cold 1X PBS using a 29G1/2 syringe. The lysates were inactivated at 70°C for 10 minutes, then centrifuged at maximum speed at 4°C. Thirty microliters of the lysate were mixed with 170 µl of Autokit Glucose reagent. The plates were incubated at 37°C for 30 minutes, and absorbance was measured at 600 nm. Glucose concentrations were determined based on the absorbance values recorded for glucose standards. For Trehalose measurement from hemolymph, 2 µl of hemolymph was diluted 5 times, and 8 µl of this diluted hemolymph was incubated with 5 µl 8x porcine kidney trehalase

(sigma) at 37°C overnight. 10 µl of this mix was used for glucose measurement, as described above.

HepG2 Cells – Knockdown and Overexpression Strategies

HepG2 cells were purchased from ATCC and maintained in EMEM supplemented with 10% FBS and 1% PenStrep at 37°C in a 5% CO_2 atmosphere.

For inducible overexpression of human MPC1 and MPC2, the HA-MPC2-P2A-T2A-MPC1-FLAG sequence was cloned into the pLVX-TetOne-Zeocin vector. Lentiviral particles were generated using Gag-Pol, pMD2.G, and VSVG packaging plasmids.

Viral particles were produced by co-transfecting 293T cells with the respective packaging plasmids using polyethylenimine (PEI, Sigma, #765090) as the transfection reagent at a 3:1 mass ratio of PEI to DNA. The virus-containing medium was collected 48 hours post-transfection, filtered through a 0.45 µm filter, and added to HepG2 cells cultured in normal medium, along with polybrene (Sigma, #P1240000) at a concentration of 10 µg/ml. Transduced cells were selected with 10 µg/ml Zeocin (Gibco, #R25001) for 1 week, and the level of overexpression was assessed by western blotting.

For PC over-expression, PC coding sequence was amplified from mRNA isolated from HepG2 cells using primers 5' GAATTC ATGCTGAAGTTCCGAACAGTCCATGGG, 3' GGATCC CTCGATCTCCAGGATGAGGTCGTCACC and cloned into pLenti-CMV-Blast. Similarly, SLC1A3 cDNA was amplified with primers 5' GGATCC ATGACTAAAAGCAATGGAGAAGAGC, 3' CTACATCTTGGTTTCAATGTCGATGG and GOT2 coding sequence was amplified using primers 5' GGATCC ATGGCCCTGCTGCACTCCGG, 3' TCTAGA CTTGGTGACCTGGTGAATGGCATGG and cloned in pLenti-CMV-Blast (addgene, #17486). The coding sequences of NDI (addgene, #72876) and d2GFP (addgene, #115665) were also cloned into pLenti-CMV-Blast vector. Cells were selected on 3 µg/ml blasticidin (Gibco, A1113903) for 3 days. To generate knock out cells, following gRNAs were used. PCg5e-GAAGCCTATCTCATCGGCCG *CGG,* PCg6e- CGAAGTCCGCTCGCTCAGAG *AGG*, PEPCK2g2e-ATCTCCACTAAGCACTCGCA *GGG*, PEPCK2g3e-CATGCGTATTATGACCCGAC *TGG*, GOT2ga- GAGTGGCCGGGTAAGCTGAGCAG *AGG*, GOT2gb-GGAGTGGACCCGCTCCGGAACAG *TGG*. The guides were annealed and clones in lentiCRISPRv2 with blasticidin (addgene, #83480) resistance using BsmBI.

HepG2 Cells and 2D Cell Size Analysis

HepG2 cells were cultured on 12 mm coverslips in a 24-well plate at a low density of 10,000 cells per well in Human Plasma-Like Medium (Gibco, #A4899101) supplemented with 10% FBS

(Sigma, F0926) and 1% PenStrep (Thermo, #15140). The next day, treatments were initiated as described in the figure legends, including 1 µg/ml doxycycline (Sigma, #D5207), 10 µM UK5099 (Sigma, PZ0160-5MG), 10 mM glycine (Sigma, #G7403), 5 mM alanine (Sigma, #A7469), 5 mM asparagine (Sigma, #A4159), 5 mM aspartic acid (Sigma, #A7219), 5 mM glutamic acid (Sigma, #G8415), 5 mM proline (Sigma, #P5607), 5 mM serine (Sigma, #S4311), 10 µM AZD7545 (MedChemExpress, #HY-16082), 1 mM dichloroacetate (Sigma, #347795), 100 nM duroquinone (Sigma, #D223204), and 2 nM gramicidin (Sigma, #G5002).

For time-course experiments in Figure 3, cells were fixed at 2, 4, 6, 8, 10, 12, 18, and 24 hours after doxycycline treatment using 4% paraformaldehyde in 1X PBS for 20 minutes at RT. For all other experiments, cells were fixed 24 hours after doxycycline treatment. Following fixation, cells were washed once with 0.1% PBT (0.1% Triton X-100 in 1X PBS) for 10 minutes and incubated with Rhodamine Phalloidin at a 1:400 dilution in 1X PBS buffer for 20 minutes at RT. After a couple of washes in 1X PBS, cells were mounted in DAPI-supplemented VectaShield.

Images were captured using a fluorescence microscope (Carl Zeiss, Axio Vision) focusing on the plane of the cellular nuclei at 20X magnification, where all nuclei were in focus, and the 2D area of HepG2 cells was measured using FIJI software. All cell size analyses were conducted in a blinded manner.

For 3D cell volume analysis, images were captured using a Laser Scanning Confocal Microscope (LSM 880, Carl Zeiss). The red fluorescence signal was used for 3D reconstruction, and cell volume was measured using an ImageJ Macro code in FIJI.

Measurement of Protein Synthesis in HepG2 Cells

HepG2 cells were cultured in either 2D monolayers or spheroid forms. At the desired time point, cells were treated with 20 µg/ml puromycin (Sigma, #P4512) in Human Plasma-Like Medium (HPLM) for 30 minutes at 37°C. Following treatment, cells were washed with 1X PBS, and proteins were extracted using 1X RIPA buffer at 4°C. Protein concentrations were quantified, and 15 µg of total protein was separated by SDS-PAGE using standard methods. Proteins were then transferred onto a nitrocellulose membrane, and puromycin-labeled peptides were detected using an anti-puromycin [3RH11] antibody (Kerafast, #EQ0001) followed by incubation with an appropriate secondary antibody.

Protein synthesis in HepG2 cells was also analyzed using the Click-iT HPG Alexa Fluor 594 kit (Molecular Probes, #C10429). HepG2 cells were grown on 12 mm coverslips at a density of 10,000 cells per well and treated with 1 µg/ml doxycycline for 24 hours. Cells were then incubated with 50 µM L-homopropargylglycine (HPG) in methionine-free DMEM (Gibco,

#21013024) for 30 minutes at 37°C. After incubation, cells were washed twice with 1X PBS for 2 minutes each and fixed in 4% paraformaldehyde for 20 minutes at room temperature.

For OPP staining, appropriately fixed cells were washed twice with 0.1% PBT (0.1% Triton X-100 in 1X PBS) supplemented with 0.5% bovine serum albumin (BSA) for 10 minutes each. HPG was detected using the Click-iT reaction mixture, which included 88 µl of OPP Reaction Buffer, 20 µl of copper solution (component D), 2.5 µl of component B, and 100 µl of Buffer Additive (component E), following the manufacturer's instructions. Cells were washed twice in Reaction Rinse Buffer for 10 minutes each, followed by two washes in 0.1% PBT supplemented with 0.5% BSA for 10 minutes each at room temperature. After a final wash in 1X PBS, the coverslips were mounted in DAPI-supplemented Vectashield. Images of the cells were captured using a confocal microscope (LSM 880, Zeiss).

Analysis of Spheroids

HepG2 cells were cultured in ultra-low attachment 96-well plates (Costar, #7007) at a density of 10,000 cells per well in Human Plasma-Like Medium (HPLM) supplemented with 10% FBS and 1% penicillin-streptomycin. Treatments were applied as specified in the figure legends, including 1 µg/ml doxycycline, 5 mM aspartate, 5 mM glutamate, 10 µM UK5099, MEM non-essential amino acids (Gibco, #11140050), 100 nM nicotinamide riboside (Sigma, #SMB00907), and 10 µM NMN (Sigma, #N3501). Cells were incubated for 6 days at 37°C with CO2 and O2. Brightfield images of the spheroids were captured using a Zeiss Axio Observer Z1 microscope, and spheroid size was measured using FIJI software.

To quantify cell numbers, 12 spheroids from each condition (EV or MPC+) were pooled, dissociated by trypsinization, and the number of cells was counted using a CellQuant system (Bio-Rad).

For cell cycle analysis, cells were stained using Vybrant® DyeCycle™ Violet stain (Molecular Probes, #V35003). After pooling and dissociating 12 spheroids from each condition (EV or MPC+), cells were centrifuged and resuspended in 200 µL of 5 µM Vybrant® DyeCycle™ Violet stain in EMEM supplemented with 10% FBS. The staining was performed by incubating the cells at 37°C for 30 minutes, protected from light. Samples were analyzed using a BD Celesta flow cytometer with ~405 nm excitation and ~440 nm emission. The resulting FCS files were processed in FlowJo software, where the forward scatter of singlets was recorded, and median data were used to plot graphs. Vybrant dye staining was employed to assess the distribution of cells in the G1, S, and G2/M phases.

For apoptosis detection, an Annexin V/PI staining kit (Molecular Probes, #V13241) was used, with 5 µM camptothecin (MedChemExpress, #HY-16560) serving as a positive control. Sixteen

spheroids were collected, dissociated with trypsin as described above, and resuspended in 200 µL of 1X annexin-binding buffer. Cells were incubated with 1 µl of Alexa Fluor™ 488 Annexin V (Component A) and 0.2 µl of 100 µg/ml PI working solution at room temperature for 15 minutes. Stained cells were then analyzed using a BD Canto flow cytometer, measuring fluorescence emission at 530 nm and 575 nm (or equivalent) with 488-nm excitation.

Biomolecule Separation and Measurement

For this experiment, biomolecules were extracted and measured from both *Drosophila* larvae fat bodies and HepG2 cell spheroids. Fat bodies were dissected from 10 male larvae at 120 hours after egg laying (AEL) and collected in 150 µl of 1X PBS. The samples were lysed by performing three freeze-thaw cycles. A total of 24 spheroids were homogenized in 150 µl of radioimmunoprecipitation assay (RIPA) buffer (50 mM Tris-HCl, 1% NP-40, 0.5% sodium deoxycholate, 0.1% SDS, 150 mM NaCl, and 2 mM EDTA).

Lysates were centrifuged at 7500 × g for 5 minutes to remove debris. The resulting supernatant was used for the following measurements. Triglyceride Measurement- For triglyceride analysis, 30 µL of the supernatant was incubated for 10 minutes at 75°C. Following this, 10 µl of homogenate from the spheroids or 2 µL from fat bodies was added to 200 µl of Triglycerides Reagent (Thermo Fisher Scientific, #TR22421). The mixture was incubated for 10 minutes at 37°C in 96-well microplates with gentle shaking. Absorbance was measured at 550 nm using the Synergy Neo2 multimode plate reader (BioTek).

Protein Measurement- Protein concentrations were determined by mixing 2 µl of the supernatant with 200 µl of BCA Protein Assay Reagent (Thermo Scientific, #23225). The mixture was incubated for 30 minutes at 37°C with gentle shaking in 96-well microplates. Absorbance was measured at 560 nm.

RNA and DNA Separation**-** The remaining 100 µl of the supernatant was processed for RNA and DNA separation using TRIzol reagent (1 ml; Invitrogen, # 15596026). To separate RNA, 0.2 ml of chloroform was added to the sample, followed by centrifugation at 12,000 × g for 15 minutes at 4°C. The RNA in the interphase was purified using 75% ethanol, following standard methods, and quantified using a NanoDrop spectrophotometer. DNA was extracted from the organic phase by adding 100% ethanol, followed by isopropanol precipitation. The resulting pellets were washed with 0.3 M guanidine hydrochloride in 95% ethanol, resuspended in 0.1 M sodium citrate in 10% ethanol (pH 8.5), and washed with 75% ethanol. Finally, the DNA pellets were resuspended in 0.1 ml of 8 mM NaOH by pipetting. The pH was adjusted to 7.2 with HEPES, and the DNA was quantified using a NanoDrop spectrophotometer.

Measurement Of NADH/NAD$^+$ Protocol

For HepG2 cells, 1x10^6 cells treated with 1ug/ml dox for 24 hours were scraped in 1.5 ml tube. For NADH/NAD$^+$ ratio analysis from spheroids, 18 spheroids were treated with 1ug/ml dox for 6 days,and then resuspended in 1mL 1XPBS. Scraped cells or pooled spheroids were centrifuged (13,500x*g*, 10 s, 4°C) and resuspended in 250 ul lysis buffer. Fat bodies from 10 male larvae were dissected in 1X PBS and resuspended in the lysis buffer provided with kit. To separate cytoplasmic and mitochondrial fractions by rapid subcellular fractionation, lysates were centrifuged (13,500x*g*, 10 s, 4°C) and the supernatant was collected for the cytosolic fraction, while the remaining pellet contained the mitochondria. Mitochondrial pellet was resuspended in 100 ul lysis buffer.

NADH to NAD+ ratios were measured using Amplite Fluorimetric NAD$^+$/NADH ratio assay kit (AAT Bioquest, #15263) as directed by the instructions provided. Briefly, 25uL of cytoplasmic or mitochondrial fractions were mixed with either NADH or NAD$^+$ extraction solution. Samples were incubated at 37°C for 15 minutes. Later, 25ul of either NAD$^+$ or NADH extraction was added, which was followed by incubation with 75ul mix of NADH sensor buffer and NAD$^+$/NADH recycling enzyme for 1 hour at RT. Fluorescence intensity was recorded at 540 nm excitation and 590 nm emission.

Protein Extraction and Western Blotting

HepG2 cells were directly scraped into RIPA supplemented with protease and phosphatase inhibitors (Roche Molecular, #04906845001). For spheroids, 18 spheroids were pooled, washed with 1X PBS, and then incubated in RIPA buffer with the protease and phosphatase inhibitor cocktail. After 45 minutes on ice with vortexing every 15 minutes, lysates were centrifuged at 16,000xg for 15 minutes at 4°C to remove insoluble material.

Protein concentration was measured using the Bicinchoninic Acid (BCA) protein assay (Thermo Fisher Scientific, 23225). Samples were mixed with 4x sample loading buffer and heated at 95°C for 5 minutes. Protein samples (15 µg) were separated on SDS-polyacrylamide gel electrophoresis (SDS-PAGE) at 20 mA per gel, transferred onto a 0.45 µm nitrocellulose membrane (GE Healthcare) using the Mini Trans-Blot module (Bio-Rad) at 120 V for approximately 2 hours.

The membrane was blocked with 5% non-fat milk (Serva) in Tris-buffered saline with 0.05% Tween 20 (TBS-T) for 1 hour. It was then incubated overnight with primary antibodies diluted in TBS-T. The next day, the membrane was washed with TBS-T and incubated with fluorophore-conjugated secondary antibodies in TBS-T for 1 hour. Following additional washes with TBS-T,

fluorescence was detected using the Odyssey CLx imaging system (LI-COR Biosciences) and analyzed using FIJI software. Antibodies used are listed in Appendix 1.

Steady-State Metabolomic Studies

10 million HepG2 cells with MPC+ and EV control expression were grown in 2D culture were treated with 1ug/ml dox in HPLM supplemented with 10% HPLM. After 24 hours, the culture medium was collected and quenched with 1:4 volume of 100% methanol. Cells were washed and quenched with 1 ml of 80% methanol in water. Cell lysates were then subjected to three rapid freeze-thaw cycles and then spun at 16,000x*g* for 10 min at 4°C. The supernatants were evaporated using a SpeedVac concentrator. Each sample or treatment had 4 to 5 replicates.

^{13}C-glucose tracing for M+3 vs M+2 ratio of TCA cycle metabolism

10 million HepG2 cells with MPC+ and EV control expression were grown in 2D culture and were treated with 1ug/ml dox in HPLM. After 24 hours, the culture medium was changed to ^{13}C-glucose tracing media: glucose-free HPLM supplemented with 4.5g/L ^{13}C glucose and 10% dialyzed FBS. 0 hour, 1 hour, 2 hours, and 4 hours later, cells were washed and quenched with 1 ml of 80% methanol in water. Cells were scraped out in Methanol, and lysates were then subjected to three rapid freeze-thaw cycles and then spun at 16,000x*g* for 10 min at 4°C. The supernatants were evaporated using a SpeedVac concentrator.

^{13}C-Lactate Tracing for Gluconeogenesis Assay

10 million HepG2 cells with MPC+ and EV control expression were grown in 2D culture were treated with 1ug/ml dox in DMEM without glucose, without glutamine (Gibco, #A1443001) with 10% dialyzed FBS. After 16 hours, culture medium was replaced with 6 ml of 1ug/ml dox in DMEM without glucose, without glutamine and without FBS. 3 hours later, culture medium was replaced with 6 ml of 1ug/ml dox and 20mM lactate (Sigma, #490040) containing DMEM without glucose or glutamine or FBS. After 4 hours, 300 µl culture medium was collected and quenched with 1:4 volume of 100% methanol. Cells were washed and quenched with 1 ml of 80% methanol in water. Cell lysates were then subjected to three rapid freeze-thaw cycles and then spun at 16,000x*g* for 10 min at 4°C. The supernatants were evaporated using a SpeedVac concentrator. Each cell types had 4 to 5 replicates.

Gas Chromatography-Mass Spectrometry Derivatization

Dried metabolites were derivatized and prepared for Gas chromatography following standard methods. Dried samples were resuspended in 30 µl of anhydrous pyridine with methoxamine hydrochloride (10 mg/ml) and incubated at RT overnight. The next day, the samples were heated at 70°C for 15 min and centrifuged at 16,000*g* for 10 min. The supernatant was

transferred to a pre-prepared gas chromatography-mass–mass spectrometry autoinjector vial with 70 µl of *N*-(*tert*-butyldimethylsilyl)-*N*-methyltrifluoroacetamide (MTBSTFA) derivatization reagent. The samples were incubated at 70°C for 1 hour, after which aliquots of 1 µl were injected for analysis. Samples were analyzed using either an Agilent 6890 or 7890 gas chromatograph coupled to an Agilent 5973N or 5975C Mass Selective Detector, respectively. The observed distributions of mass isotopologues of glucose, pyruvate, citrate, succinate, aspartate, glutamate, malate, fumarate, and phosphoenolpyruvate were corrected for natural abundance.

Liquid chromatography-mass spectrometry

Following standard methods, dried metabolites were resuspended in 100 µl of 0.03% formic acid in analytical-grade water, vortexed, and centrifuged to remove insoluble material. 20 µl of supernatant was collected and injected to AB SCIEX QTRAP 5500 liquid chromatography/triple quadrupole mass spectrometer (Applied Biosystems SCIEX). Chromatogram review and peak area integration were performed using MultiQuant (version 2.1, Applied Biosystems SCIEX). The peak area for acetyl CoA, ADP, ATP, NAD^+, NADH was normalized against the total ion count of that sample.

Oxygen consumption rate

Oxygen consumption rates (OCR) were measured using an XFe96 Extracellular Flux Analyzer (Agilent) according to the manufacturer's instructions. Cells were plated at a density of 60,000 cells per well in Seahorse microplates (Agilent) and allowed to adhere for 6 hours. MPC was induced with 1 µg/ml doxycycline overnight. Afterward, the cell culture media was removed and replaced with Seahorse assay media, which consisted of DMEM supplemented with 4 mM glutamine. OCR was assessed under basal conditions and following sequential injections of 1 mM glucose, oligomycin (2 µM), FCCP (0.5 µM), and a mix of rotenone plus antimycin A (2 µM each). Immediately after the measurements, cells were lysed in RIPA buffer, and the protein concentration was used to normalize the OCR data.

Primary Hepatocyte Cultures and Analysis

Rat primary hepatocytes (Lonza, #RWCP01) were thawed and plated in a 24-well plate at a density of 0.16 million cells per well in Hepatocyte Plating Medium (Lonza, #MP100). Four hours post-plating, the medium was replaced with Hepatocyte Basal Medium (HBM) supplemented with BCM SingleQuots (Lonza, #CC-4182), including Bovine Pituitary Extract (BPE), Insulin, Hydrocortisone, Gentamicin/Amphotericin-B (GA), Transferrin, and human Epidermal Growth Factor (hEGF).

Twenty-four hours after plating, the hepatocytes were transfected with 1 µg of either pT3.GFP or pT3.MPC2Flag-P2AT2A-MPC1HA using Lipofectamine 3000 (Invitrogen, #L3000001). Forty-eight hours post-transfection, cells were lysed in 1X RIPA buffer, and Western blot analysis was performed to confirm the overexpression of MPC1 and MPC2.

Forty-eight hours post-transfection, hepatocytes were fixed in 4% paraformaldehyde in 1X PBS. Following several washes with 0.1% PBT, cells were incubated in 5% BSA and stained with anti-MPC1 antibody overnight at 4°C. MPC1 was detected using a secondary anti-rabbit Alexa Fluor antibody. Cells were also stained with Phalloidin Red. Coverslips were mounted in DAPI-supplemented Vectashield, and images were captured using an LSM 880 confocal microscope. Cell area marked by Phalloidin Red was quantified using differential interference contrast filter and analyzed with FIJI software.

For protein synthesis measurement, hepatocytes were incubated with 20 µg/ml puromycin for 30 minutes. Puromycin-tagged peptides were visualized by immunostaining with rabbit anti-puromycin antibody (1:500) and mouse anti-Flag M2 antibody (1:1000, Sigma, F1800), followed by the appropriate secondary antibodies. Images were captured with the LSM 880 confocal microscope. Puromycin intensity was measured using FIJI, and the percent change in puromycin intensity in Flag-positive cells was compared to Flag-negative cells.

Gluconeogenesis was assessed using lactate and pyruvate as substrates. Forty-eight hours post-transfection, hepatocytes were incubated in low-glucose DMEM with 1 mM sodium pyruvate and 4 mM glutamine without FBS. After 16 hours, hepatocytes were treated with 200 ng glucagon in no-glucose DMEM without FBS for 3 hours. Cells were then cultured in media with 20 mM lactate and 2 mM pyruvate, with and without 10 µM UK5099, for 2 and 4 hours. Glucose levels in the media were measured using the Amplex Red Glucose Assay Kit (Invitrogen, #A22189) according to the manufacturer's instructions. Glucose production per cell per hour was plotted on a graph.

The compartmentalized NADH to NAD^+ ratio in hepatocytes was quantified 48 hours post-transfection using the Amplite Fluorimetric NAD^+/NADH Ratio Assay Kit as described previously.

Figure Legends

Figure 1: Increased mitochondrial pyruvate transport reduces size of *Drosophila* fat body cells.

a-b. a) A schematic representation of *Drosophila* developmental stages with specified time points (hours after egg laying (AEL) at 25°C) at which larvae were dissected to collect fat

bodies. **b)** Representative images of larval fat bodies at the indicated times (hours AEL) stained with rhodamine phalloidin to visualize cell membranes and DAPI to visualize DNA. The scale bar represents 25 µm.

c. Quantification of fat body cell area based on rhodamine phalloidin stained cell membranes at the indicated time points. Data are presented as mean ± standard deviation (s.d.) from six biological replicates, with each replicate averaging the size of 50 randomly selected cells from fat bodies dissected from five male larvae.

d-e. d) A schematic of pyruvate metabolism. In the cytoplasm, pyruvate is a product of glycolysis, synthesized by Pyruvate Kinase (Pyk) or from lactate via Lactate Dehydrogenase (LDH). Pyruvate is transported into mitochondria by the Mitochondrial Pyruvate Carrier (MPC) complex. Within mitochondria, pyruvate is converted into acetyl-CoA by Pyruvate Dehydrogenase (PDH) or into oxaloacetate by Pyruvate Carboxylase (PC), both of which are substrates for the TCA cycle. PEPCK2 converts oxaloacetate into phosphoenolpyruvate. **e)** *Pyk*, *Mpc1*, *Mpc2, Pdha* and *Dlat* transcripts were quantified from larval fat bodies collected at the indicated times.

f-g. f) Representative confocal microscope images of phalloidin- and DAPI-stained fat bodies with flip-out Gal4 clones expressing MPC1-P2A-MPC2 (MPC+), marked with GFP at 120 hours AEL. The images at the bottom show magnified insets of GFP-positive cells in control and MPC expressing clones. **g)** Quantification of GFP-positive clonal cell area with the indicated genetic manipulations- control, MPC+ and *Mpc1*-KD. Data are presented as mean ± s.d. from six biological replicates, with each set averaging the size of 20 clonal cells from fat bodies collected from five male larvae.

h-i. h) Images showing control and MPC+ clones from larvae ~~f~~ed on no sugar diet. **I)** Quantification of the area of control, MPC+ and *Mpc1*-KD fat body clonal cells from larvae fed on a diet containing either 9% sugar or no sugar.

j. Quantification of the area of MPC+ fat body clonal cells from larvae fed a diet supplemented with or without 20 µM UK5099.

k. Fold change of the abundances of the indicated macromolecules in fat bodies expressing MPC (MPC+) in all fat body cells using CG-Gal4. The abundance of each individual macromolecule is normalized to that of the respective macromolecular abundance in GFP expressing, control fat bodies. Data are represented as mean ± s.d. from three biological replicates with fat bodies collected from 10 larvae at 120 hours AEL.

l-m. l) Representative images of fat body clones stained with O-propargyl-puromycin (OPP, 20 µM for 30 minutes), showing control and MPC expressing GFP-positive cells. The top panels

show GFP-positive clones and OPP staining in red, while the bottom panels show respective OPP channel. Arrows indicate cells with the specified genetic manipulation. The scale bar represents 20 µm. **M)** Quantification of OPP fluorescence intensity of control or MPC+ fat body cells compared to neighboring non clonal cell. Data are presented as mean ± s.d. from six biological replicates, with each set averaging the size of 20 clonal cells from fat bodies collected from five male larvae.

Unpaired t-tests or one-way ANOVA tests were performed to evaluate the statistical significance of the data, with p-values mentioned in the graphs where significance was noted.

Supplementary Figure 1: Transcriptomic changes in fat body during larval development (related to Main Figure 1).

a. A heatmap displaying changes in mRNA abundance of genes encoding mitochondrial proteins and enzymes involved in various metabolic pathways in wild type- w^{1118} fat bodies collected at the specified time points. Right. Clustered hallmarks are indicated by a color gradient corresponding to relative gene expression levels.

b. A heatmap illustrating transcriptomic changes in signaling pathways in w^{1118} fat body cells during *Drosophila* larval development.

c. Quantification of *Pepck* and *Pepck2* transcripts from larval fat bodies collected at the indicated times.

Supplementary Figure 2 – Increased mitochondrial pyruvate transport reduces size of *Drosophila* fat body cells. (Related to Main Figure 1)

a. Schematic representation of experimental time course using temperature-sensitive $Gal80^{ts20}$ to control Gal4 expression. At 18°C, $Gal80^{ts20}$ is active, inhibiting Gal4 expression; at 29°C, $Gal80^{ts20}$ is inactive, allowing Gal4 expression. The temperature switch occurs towards the end of the 2nd instar stage so that MPC expression construct is induced temporally only during the 3rd instar stage. Fat bodies were collected at the specified time points.

b. Quantification of *Mpc1* and *Mpc2* transcripts from fat bodies of CG-Gal4>MPC+ versus CG-Gal4>GFP or control larvae, dissected at the indicated times after the induction of Gal4 activity.

c. Quantification of fat body cell area in MPC+ (CG-Gal4>MPC+) versus control (CG-Gal4>GFP) larvae at the indicated times after Gal4 induction. Data are presented as mean ± s.d. from six biological replicates, with each replicate representing the average size from 50 randomly selected cells from fat bodies dissected from five male larvae.

d. Schematics illustrating the use of the Ay-Gal4 cassette to generate clones with MPC expression. Clones are generated by leaky expression of hs-flp1.22-flippase, which binds to specific FRT sites in chromatin, leading to the excision of the spacer *'yellow'* gene and positioning of the *actin5C* promoter next to the Gal4 coding sequence. This is followed by Gal4 expression in the cell and subsequent expression of UAS-GFP or UAS-MPC1-P2A-MPC2 constructs. Due to the leaky and random expression of the flippase, GFP-marked mosaicism occurs in only 1-5% of fat body cells.

e-f. Representative images of fat bodies with MPC expression and control clones, showing increased abundance of (**e)** MPC1 and (**f)** MPC2 proteins. Arrows indicate cells with the specified genetic manipulation. The scale bar represents 20 µm.

g. Representative images of fat bodies with MPC+ and control clones dissected from larvae fed on a diet supplemented with 20 µM UK5099. Arrows indicate cells with the specified genetic manipulation. The scale bar represents 20 µm.

h-k. The abundances of **(h)** DNA, **(i)** RNA, **(j)** triacylglycerides (TAGs), and **(k)** protein in fat bodies where MPC is expressed in all fat body cells using CG-Gal4 driver. The abundance of each individual macromolecule is normalized to that of the control. Data are represented as mean ± s.d. from three biological replicates with fat bodies collected from ten larvae at 120 hours AEL.

l-n. l) Representative images of MPC+ and control fat body clones showing lipid droplets stained with LipidTox in red. The area in square is presented in high-magnification insets below to show lipid distribution in the clonal cells. The scale bar represents 25 µm. **m)** Quantification of lipid droplets relative to cell size in MPC+ versus control cells. **n)** The data are presented as the number of lipid droplets per cell area and the fraction of cell area covered by lipid droplets.

o-p. o) Representative EdU-stained confocal images of MPC+ and control fat body cells, showing replicating DNA. Arrows indicate cells with the specified genetic manipulation. The scale bar represents 20 µm. **p)** Quantification of total EdU fluorescence intensity in GFP-positive cells compared to neighboring GFP-negative cells in MPC+ versus control clones. Data are presented as mean ± s.d.

Unpaired t-tests were performed to evaluate the statistical significance of the data, with p-values noted in the graph if significance was observed.

Figure 2: mTORC1 and Myc pathways are hyperactivated in MPC overexpressing fat body cells.

a. Schematic of the mTORC1 pathway. The mTORC1 pathway is activated by pro-growth signals such as insulin, leading to the phosphorylation of S6 kinase (S6K) and 4EBP. S6K phosphorylates ribosomal protein S6, while 4EBP phosphorylation inactivates 4EBP and releases elongation factor eIF4E. These events increase ribosomal assembly and elongation rates, thereby enhancing protein synthesis.

b-c. **b)** Representative images of fat body clones with *S6k* over-expression, control clones, and MPC+ clones, stained for phosphorylated S6 (p-S6) in red (top panels) and white (bottom panels). Arrows indicate clonal cells with the specified genetic manipulation. The scale bar represents 20 µm. **c)** Quantification of total p-S6 fluorescence intensity in GFP-positive cells compared to neighboring GFP-negative cells in MPC+ versus control clones. Data are presented as mean ± s.d. with statistical significance as scored with One-way Annova test.

d-e. **d)** Representative images of fat body clones with *Rheb* over-expression, control clones, and MPC+ clones stained for phosphorylated 4EBP (p-4EBP) in red (top panels) and white (bottom panels). Arrows indicate clonal cells with the specified genetic manipulation. The scale bar represents 20 µm. **e)** Quantification of total p-4EBP fluorescence intensity in MPC+ versus control clones with statistical significance as scored with One-way Annova test.

f-g. f) Representative images of fat body clones with *Myc* knockdown, control clones, and MPC+ clones stained for Myc protein in red (top panels) and white (bottom panels). Arrows indicate clonal cells with the specified genetic manipulation. The scale bar represents 20 µm. **g)** Quantification of total Myc fluorescence intensity in MPC+ versus control clones with statistical significance as scored with One-way ANOVA test.

h-i. **h)** Representative images of fat body clones from starved wild type, control clones, and MPC+ clones, stained for phosphorylated eIF2α (p-eIF2α) in red (top panels) and white (bottom panels). Arrows indicate clonal cells with the specified genetic manipulation. The scale bar represents 20 µm. **i)** Quantification of total p-eIF2α fluorescence intensity in MPC+ versus control clones with statistical significance as scored with One-way ANOVA test. Data are presented as mean ± s.d.

One-way ANOVA tests were performed to evaluate the statistical significance of the data, with p-values noted in the graph if significance was observed.

Supplementary Figure 3: mTORC1 and Myc pathways are hyperactivated in MPC overexpressing fat body cells. (Related to Main Figure 2)

a. Representative images of fat body clones with PI3K-DN (dominant-negative) expression, control clones, and MPC+ clones stained for dFoxo in red (top panels) and white (bottom

panels). Arrows indicate clonal cells with the specified genetic manipulations. The scale bar represents 20 µm.

b. Transcriptomic analysis of MPC+ fat bodies compared to control, represented as Hallmarks from GSEA (Gene Set Enrichment Analysis).

c-d. Quantification of the area of MPC+ cells with or without *PI3K* over-expression **(c),** and with or without *Tsc1* knock down **(d).** Data are presented as mean ± s.d. from five biological replicates, where each data point represents the average size of 20 clones from fat bodies collected from five male larvae.

e-f. Quantification of cell area in MPC+ clones with *Myc* over-expression **(e)** or *Myc* knockdown **(f).** Data are presented as mean ± s.d. from five biological replicates, where each data point represents the average size of 20 clones from fat bodies collected from five male larvae.

Figure 3: Increased mitochondrial pyruvate transport reduces size of HepG2 spheroids.

a. Western blots showing inducible expression of MPC1 and MPC2 at 2-hour intervals following treatment with 1 µg/ml doxycycline. Citrate synthase and tubulin were used as loading controls. Both endogenous and epitope tag bands are shown.

b. Quantification of the 2D area of HepG2 cells with MPC expression (MPC+) or empty vector (EV) fixed and stained with rhodamine phalloidin at the indicated times after doxycycline treatment. Data are presented as mean ± s.d. from five biological replicates, with each replicate representing the average size of 25 randomly selected cells.

c. Quantification of the 2D area of MPC+ or EV HepG2 cells treated with 10 µM UK5099. Data are presented as mean ± s.d. from five biological replicates, with each replicate representing the average size of 25 randomly selected cells.

d-e. d) Representative brightfield images of HepG2 spheroids with empty vector (EV) or MPC expression (MPC+) treated with 1 µg/ml doxycycline for six days. The scale bar represents 200 µm. **e)** Quantification of spheroid area from images of MPC+ or EV HepG2 spheroids, with or without doxycycline treatment. Data are presented as mean ± s.d. from 30 technical replicates.

f-g. f) Forward scatter (FSC) of cells dissociated from MPC+ (red) or EV spheroids with cell count normalized to mode. **g)** Median FSC of MPC+ HepG2 spheroids treated with or without 1 µg/ml doxycycline. Data are presented as mean ± s.d. from three biological replicates.

h. Fold change in macromolecules—DNA, TAGs, RNA, and protein—fractionated from EV or MPC+ HepG2 spheroids normalized to that in EV HepG2 cells.

i-j. i) Representative images showing L-Homopropargylglycine (HPG)-labeled newly synthesized proteins in EV or MPC+ HepG2 cells. The top panels show HPG staining, and the

lower panels show nuclei stained with DAPI. The scale bar represents 20 μm. **j)** Quantification of HPG fluorescence intensity is presented as mean ± s.d. from 35 cells, for both EV and MPC+ cells.

k-l. k) Western blot analysis of nascent protein synthesis using a puromycin incorporation assay (20 μg/ml puromycin for 30 minutes) in either EV or MPC+ HepG2 spheroids (protein lysates from 16 spheroids loaded in each lane). **l)** Quantification of 70 kD band intensity in puromycin blot normalized with tubulin band intensity and represented as mean ± s.d. from three independent experiments.

m. Relative accumulation of destabilized GFP (d2GFP) in EV or MPC+ HepG2 spheroids treated with or without 1 μg/ml doxycycline ± 10 μM UK5099. Data are presented as mean ± s.d. from three biological replicates.

Unpaired t-tests, one-way, or two-way ANOVA tests were performed to evaluate the statistical significance of the data, with p-values noted in the graph if significance was observed.

Supplementary Figure 4: MPC overexpression reduces size of HepG2 cells in 2D and spheroid culture (Related to Main Figure 3).

a. Quantification of cell volume from confocal images of HepG2 cells expressing MPC (MPC+) or an empty vector (EV). Data is presented as mean ± s.d. from 22 EV cells and 25 MPC+ cells.

b. Quantification of the number of cells per spheroid in EV or MPC+ HepG2 cells with or without doxycycline treatment. Data is presented as mean ± s.d. from 18 technical replicates.

c. Cell cycle profiles of MPC+ HepG2 spheroids treated with or without doxycycline treatment. Data is presented as mean ± s.d. from three biological replicates.

d. Annexin/Propidium Iodide (PI) analysis of MPC+ HepG2 cells cultured with or without doxycycline. Data is presented as mean ± s.d. from three biological replicates.

e-h. Concentrations of **(e)** DNA, **(f)** RNA, **(f)** triacylglcyerides (TAGs) and **(g)** protein measured for 18 MPC+ and 18 EV HepG2 cells. Data is shown as mean ± s.d. from three biological replicates.

Unpaired t-tests and one-way ANOVA tests were performed to evaluate the statistical significance of the data, with p-values mentioned in the graph if significance is noted.

Figure 4: Increased mitochondrial pyruvate metabolism promotes gluconeogenesis via Pyruvate Carboxylase to suppress protein synthesis.

a. Schematic illustration of the ^{13}C-glucose tracing strategy used to measure the activity of Pyruvate Dehydrogenase (PDH) and Pyruvate Carboxylase (PC). TCA metabolites labeled with

two heavy carbons (^{13}C or M+2 TCA pool) result from PDH activity, whereas M+3 TCA metabolites result from PC activity. PDH is inhibited by PDK-mediated phosphorylation. DCA and AZD7545 are inhibitors of PDK.

b. Fractional enrichment of M+2 succinate in empty vector (EV; red) and MPC expressing (MPC+; blue) HepG2 cells at the indicated times after ^{13}C-glucose tracing. MPC expression was induced for 24 hours by treatment with 1 µg/ml doxycycline and media was changed to ^{12}C-glucose. The change in M+2 succinate is significant (by two-way ANOVA test) at one hour after ^{13}C glucose incubation.

c. Fractional enrichment of M+3 succinate in EV (red) and MPC+ (blue) HepG2 at the indicated times after ^{13}C-glucose tracing. MPC expression was induced for 24 hours by treatment with 1 µg/ml doxycycline. The change in M+3 succinate is significant (by two-way ANOVA test) at four hours after ^{13}C-glucose incubation.

d. Rate of oxygen consumption (OCR) in EV and MPC+ HepG2 cells.

e-f. e) Representative images of phalloidin- and DAPI-stained fat body cells. Arrows indicate GFP-positive clones with MPC expression (MPC+), *Pcb* knock down with MPC expression (MPC+, *Pcb*-KD) or *Pcb* overexpression (*Pcb*+). The scale bar represents 20 µm. **f)** Quantification of the area of GFP-positive clones with control, MPC+, *Pcb* over-expression (*Pcb*+), *Pcb* and MPC co-expression (MPC+, *Pcb*+), *Pcb* knock down (*Pcb*-KD) and *Pcb* knock down with MPC expression (MPC+, *Pcb*-KD) shown as mean ± s.d. of five biological replicates, with each group representing the analysis of 20 the indicated clonal cells.

g-h. Concentration of glucose in the fat body **(g)** and concentration of glucose and trehalose in hemolymph **(h)** of larva with fat body-specific expression MPC or control. Data is presented as mean ± s.d. of three biological replicates analyzed by unpaired t-tests.

i-k. **i)** Schematic illustration of the strategy to analyze gluconeogenesis from ^{13}C-lactate. Cells convert ^{13}C-lactate into ^{13}C-pyruvate, which is transported into mitochondria by the MPC. PC converts ^{13}C-pyruvate (M+3) into oxaloacetate (M+3). PEPCK2 converts oxaloacetate (M+3) into phosphoenolpyruvate (M+3), which is converted into M+6 glucose and excreted from cells. **j)** Relative abundances of M+3 phosphoenolpyruvate (PEP) in EV and MPC+ HepG2 cells and **k)** M+6 glucose in their respective media following treatment with 20 mM ^{13}C-lactate for four hours. Data is presented as mean ± s.d. of three biological replicates, each with an average of three technical replicates.

l-m. l) Representative brightfield images of EV, MPC+, and PC knockout (KO) or PEPCK2 KO with or without MPC expression HepG2 spheroids. The scale bar represents 200 µm. **m)** Quantification of spheroid area is presented as mean ± s.d. of 30 technical replicates.

n-o. n) Representative images of phalloidin- and DAPI-stained of fat body cells. Arrows indicate GFP-positive clones with MPC expression (MPC+), and *Pepck2* knockdown with MPC expression (MPC+, *Pepck2*-KD). The scale bar represents 20 µm. **o)** Quantification of the area of GFP-positive clones with MPC+, *Pepck2* knock down (*Pepck2*-KD), *Pepck2* knock down with MPC+ (MPC+, *Pepck2*-KD), *Fbp* knock down (*Fbp*-KD), *Fbp* knock down with MPC+ (MPC+, *Fbp*-KD). Data is presented as mean ± s.d. of five biological replicates, with each group analyzing 20 clonal cells of the mentioned genetic manipulations.

n-o. n) Representative images of fat body clones stained with OPP (red). Arrows indicate GFP-positive clones with MPC expression (MPC+), *Pcb* knockdown with MPC expression (MPC+, *Pcb*-KD), or *Pepck2* knockdown with MPC expression (MPC+, *Pepck2*-KD). The scale bar represents 20 µm. **o)** Quantification of OPP intensity in the indicated clones compared with adjacent wild-type cells. Data is presented as mean ± s.d.

Unpaired t-tests, one-way ANOVA tests, or two-way ANOVA tests were performed to evaluate the statistical significance of the data, with p-values mentioned in the graph if significance is noted.

Supplementary Figure 5: Surge of mitochondrial pyruvate reduced glycolysis and promotes gluconeogenesis via Pyruvate Carboxylase (Related to Main Figure 4).

a-c. Fractional enrichment and metabolite counts of M+3 3-phosphoglyceric acid **(a)**, M+3 pyruvate **(b)**, and M+3 alanine **(c)** in empty vector (EV; red) and MPC expressing (MPC+; blue)) HepG2 cells at the indicated times after ^{13}C glucose tracing.

d-e. Metabolite counts of M+2 succinate **(d)** and M+3 succinate **(e)** in EV (red) and MPC+ (blue) HepG2 cells.

f-i. Fractional enrichment and metabolite counts of M+2 fumarate **(f)** and M+2 malate **(g)** M+3 fumarate **(h)** and M+3 malate **(i)** in EV (red) and MPC+ (blue) HepG2 cells. A two-way ANOVA test showed significant differences at four hours after ^{13}C glucose tracing.

Supplementary Figure 6: Surge of mitochondrial pyruvate promotes gluconeogenesis via Pyruvate Carboxylase to suppress protein synthesis (Related to Main Figure 4).

a-c. qRT-PCR showing **a)** *Mpc1*, **b)** *Mpc2*, and **c)** *pcb* transcripts from fat bodies of control, MPC+, *Pcb* over-expression (*Pcb*+), *Pcb* and MPC co-expression (MPC+, *Pcb*+), *Pcb* knock down (*Pcb*-KD) and *Pcb* knock down with MPC expression (MPC+, *Pcb*-KD) normalized to *rp49* transcript abundance.

d. Quantification of the area of GFP-positive fat body clones with control, MPC expression (MPC+), *Pcb* knockout (*Pcb KO*), or MPC expression with *Pcb* knockout (MPC+, *Pcb* KO). Data is presented as mean ± s.d. of five biological replicates, with each group analyzing 20 clonal cells of the indicated genetic manipulations.

e. Quantification of the areas of HepG2 cells with MPC+ with or without pyruvate carboxylase (PC) knockout using two independent sgRNA guides (PCg5 and PCg6). Western blots show the efficiency of PC knockout. Data is presented as mean ± s.d. of five biological replicates, each representing 25 randomly selected cells for each indicated genotype.

f-i. qRT-PCR showing **f)** *Mpc1*, **g)** *Mpc2*, **h)** *Pdha* and **i)** *Dlat* transcripts from fat bodies of control, MPC+, *Pdha* knock down (*Pdha*-KD), *Pdha*-knock down with MPC expression (MPC+, *Pdha*- KD), *Dlat* knock down (*Dlat*-KD), *Dlat* knock down with MPC expression (MPC+, *Dlat*-KD) normalized to *rp49* transcript abundance.

j-k. j) Representative images of phalloidin- and DAPI-stained fat body cells. Arrows indicate GFP-positive clones with MPC expression (MPC+), *Pdha* knock down (*Pdha*-KD), or MPC expression with *Pdk* knock down (MPC+, *Pdk*-KD). The scale bar represents 20 µm. Right. **k)** Quantification of the areas of GFP-positive clones with control, MPC+, *Pdha* knock down (*Pdha*-KD), *Pdha*-knock down with MPC expression (MPC+, *Pdha*- KD), *Dlat* knock down (*Dlat*-KD), *Dlat* knock down with MPC expression (MPC+, *Dlat*-KD); *Pdk* knock down (*Pdk*-KD), and *Pdk* knock down with MPC expression (MPC+, *Pdk*-KD). Data is presented as mean ± s.d. of five biological replicates, with 20 clonal cells analyzed for each of the indicated genetic manipulations.

l. Quantification of the areas of MPC+ HepG2 cells treated with the PDK inhibitors AZD7545 (10 µM) or dichloroacetate (1 mM). Data is presented as mean ± s.d. of five biological replicates, with 25 randomly selected cells analyzed for each of the indicated groups.

m. Quantification of the areas of MPC+, PEPCK2 knock out HepG2 cells. Western blots show the efficiency of PEPCK2 knockout. Data is presented as mean ± s.d. of five biological replicates with 25 randomly selected cells analyzed for each of the indicated groups.

n-q. qRT-PCR showing **n)** *Mpc1*, **o)** *Mpc2*, **p)** *Pepck2,* and **q)** *Fbp* transcripts from fat bodies of MPC+, *Pepck2* knock down (*Pepck2*-KD), *Pepck2* knock down with MPC+ (MPC+, *Pepck2*-KD), *Fbp* knock down (*Fbp*-KD), *Fbp* knock down with MPC+ (MPC+, *Fbp*-KD) normalized to *rp49* transcript abundance.

r. Quantification of the area of GFP-positive control; MPC+; *Pepck2 KO*; and MPC+, *Pepck2 KO* fat body clonal cells. Data is presented as mean ± s.d. of five biological replicates, with 20 clonal cells analyzed for each of the indicated genetic manipulations.

Unpaired t-tests, one-way ANOVA tests, or two-way ANOVA tests were performed to evaluate the statistical significance of the data, and p-values are mentioned in the graph if significance is noted.

Figure 5: Redox imbalance impedes protein synthesis and cell growth from elevated pyruvate metabolism in mitochondria.

a. NADH/NAD^+ ratios from the cytoplasmic and mitochondrial fractions of control and MPC-expressing (MPC+) fat bodies. Data is presented as mean ± s.d. of six biological replicates.

b. NADH/NAD^+ ratios from the cytoplasmic and mitochondrial fractions of empty vector (EV) and MPC-expressing (MPC+) HepG2 spheroids. Data is presented as mean ± s.d. of six biological replicates.

c-d. c) Representative images of phalloidin- and DAPI-stained fat bodies. Arrows indicate GFP-positive cells with either MPC+ or MPC and *Nmnat* co-expression (MPC+, *Nmnat*+). The scale bar represents 20 µm. **d)** Quantification of the areas of GFP-positive cells with control, MPC+, *Nmnat* overexpression (*Nmnat*+), MPC and *Nmnat* co-expression (MPC+, *Nmnat*+). Data is presented as mean ± s.d. of five biological replicates, with 20 clonal cells analyzed for each of the indicated genetic manipulations.

e-f. e) Representative images of Phalloidin and DAPI-stained fat body tissues. Arrows indicate GFP-positive cells showing MPC expression (MPC+); NDI and MPC expression (MPC+, NDI+); and NDX and MPC expression (MPC+, NDX+). The scale bar represents 20 µm. **f)** Quantification of the area of GFP-positive cells with control, MPC+, NDI expression (NDI+), NDI and MPC expression (MPC+, NDI+), NDX expression (NDX+), NDX and MPC co-expression (MPC+, NDX+). Data is presented as mean ± s.d. of five biological replicates, with 20 clonal cells analyzed for each of the indicated genetic manipulations.

g-h. g) Representative bright field images of EV or MPC+ HepG2 spheroids cultured with NAD^+ supplements (100 nM nicotinamide riboside or 1 µM NMN) as indicated. The scale bar represents 200 µm. **h)** Quantification of spheroid area is presented as mean ± s.d. of 30 technical replicates.

i-j. i) Representative images MPC+ or MPC+, NDI+ GFP-positive clones and of fat body cells stained with OPP (bottom). Clonal cells are mapped with dotted lines. The scale bar represents 20 µm. **j)** Fold change in OPP intensity of 35 GFP-positive cells compared with adjacent wild-type cells. Data is presented as mean ± s.d.

k. Relative accumulation of destabilized GFP (d2GFP) in spheroids of EV or MPC+ HepG2 cells treated with NAD□ supplements (100 nM nicotinamide riboside or 1 µM NMN) as indicated.

Unpaired t-tests, one-way ANOVA tests, or two-way ANOVA tests were performed to assess the statistical significance of the data, with p-values indicated in the graph where significance was observed.

Supplementary Figure 7: Redox imbalance impedes protein synthesis and cell growth from elevated pyruvate metabolism in mitochondria. (related to main figure 5)

a-b. a) A schematic illustration of mitochondrial pyruvate metabolism and gluconeogenesis. Following are the abbreviations: PEP- phosphoenolpyruvate, F1,6BP- fructose-1, 6-bisphosphate, F6P- fructose-6-phosphate, G6P- glucose-6-phosphate, F6Pase- fructose bisphosphatase and G6PC- glucose-6-phosphatase **b)** Western blot analysis shows the expression levels of phosphorylated PDH (p-PDH), total PDH, G6PC, PEPCK2, PC, and tubulin in MPC-overexpressing (MPC+) HepG2 cells treated with 1 µg/ml doxycycline at the indicated time points.

c. Schematic illustrating the regulation of PDH, PC, and gluconeogenesis by a network of cofactors and substrates. Following are the abbreviations: 1,3 BPG- 1,3-bisphosphoglycerate, G3P- glucose-3-phosphate, PGK- phosphoglycerate kinase, GAPDH- glyceraldehyde-3-phosphate dehydrogenase.

d. Fold enrichment of acetyl-CoA in EV and MPC+ HepG2 cells. Data is presented as mean ± s.d. of three biological replicates using unpaired t-tests.

e. The ratio of ATP to ADP in EV and MPC+ HepG2 cells. Data is presented as mean ± s.d. of three biological replicates using unpaired t-tests.

f-h. Cellular concentrations of NADH **(f)** and NAD^+ **(g)** and $NADH/NAD^+$ ratios **(h)** in EV and MPC+ HepG2 cells 24 hours after treatment with 1 µg/ml doxycycline. Data is presented as mean ± s.d. of three biological replicates using unpaired t-tests.

i. Quantification of the areas of MPC+ HepG2 cells cultured with 2 nM gramicidin. Data is presented as mean ± s.d. of five biological replicates, with 25 randomly selected cells analyzed for each of the indicated groups.

j-k. j) Representative bright field images of EV or MPC+ HepG2 spheroids with NDI expression (NDI+). The scale bar represents 200 µm. **k)** Quantification of spheroid areas is presented as mean ± s.d. of 30 technical replicates. Western blots show the efficiency of MPC expression.

l. Quantification of the area of MPC-expressing HepG2 cells cultured with or without 100 nM duroquinone. Data is presented as average ± s.d. of five biological replicates, with each group consisting of 25 randomly selected cells. Data is presented as mean ± s.d. of three biological replicates.

Unpaired t-tests, one-way ANOVA, or two-way ANOVA tests were performed to assess the statistical significance, with p-values indicated in the graph where significance was noted.

Figure 6: Reduced amino acid abundance impairs size of MPC overexpressing cells.

a. A heat map of the abundances of amino acids in empty vector (EV) and MPC expressing (MPC+) HepG2 cells cultured under standard conditions. Color codes indicate relative abundances for each amino acid: Blue (low), Green (similar), and Yellow (high).

b-c. b) Representative bright field images of EV or MPC+ HepG2 spheroids cultured with 2x or 3x the recommended concentration of non-essential amino acids cocktail (NEAA). The scale bar represents 200 µm. **c)** Quantification of spheroid areas from EV and MPC+ HepG2 spheroids cultured with 2x or 3x NEAA. Data is presented as mean ± s.d. of 30 technical replicates.

d-e. **d)** Representative images of phalloidin- and DAPI-stained fat body cells from animals fed a standard diet or a diet supplemented with 5x NEAA. Arrows indicate GFP-positive clones with MPC expression (MPC+). The scale bar represents 20 µm. **e)** Quantification of the area of MPC+ fat body clonal cells. Data is presented as mean ± s.d. of five biological replicates, with each data point representing the average size of 20 clones collected from five male larvae.

f-g. f) Representative images of phalloidin- and DAPI-stained fat body cells. Arrows indicate GFP-positive MPC+ clones and MPC+ and *slimfast* over-expression (MPC+, *Slif*+). The scale bar represents 20 µm. **g)** Quantification of the area of GFP-positive clones with control, MPC expression, *Slimfast* over-expression (*Slif*+) and MPC+ clones with *Slimfast* over-expression (MPC+, *Slif*+). Data presented as mean ± s.d. of five biological replicates, with each 20 clonal cells analyzed for each of the indicated genetic manipulations.

h. Quantification of the cell areas of EV or MPC+ HepG2 cells cultured under standard conditions or with excess of the indicated amino acid—10 mM glycine, 5 mM alanine, 5 mM serine, 5 mM asparagine, 5 mM aspartic acid, 5 mM glutamic acid or 5 mM proline. Data is presented as mean ± s.d. of five biological replicates.

i-j. i) Representative images of phalloidin- and DAPI-stained fat body cells. Arrows indicated GFP-positive cells with MPC expression (MPC+), *Got2* knock down (*Got2* KD), and *Got2* over-expression with MPC expression (MPC+, *Got2*+). **j)** Quantification of the area of GFP-positive clones with control, MPC expression (MPC+), *Got2* knock down (*Got2*-KD), *Got2* knock down with MPC expression (MPC+, *Got2*-KD), *Got2* over-expression (*Got2*+) and *Got2* over-expression with MPC expression (MPC+, *Got2*+). Data is presented as mean ± s.d. of five biological replicates, with each 20 clonal cells analyzed for each of the specified genetic manipulations.

k. NADH/NAD$^+$ ratio in cells treated with 10 µM UK5099, 1 µM NMN, or 5 mM aspartate. Data is presented as mean ± s.d. of three biological replicates.

l-m. l) Western blot analysis of puromycin-labeled (20 µg/ml puromycin for 30 minutes) nascent protein in EV or MPC+ HepG2 cells cultured with 10 µM UK5099, 1 µM NMN, or 5 mM aspartate. **m)** Quantification of intensities of puromycin labeling in EV and MPC+ cell lysates.

Unpaired t-tests and one-way ANOVA tests were performed to evaluate the statistical significance of the data, and p-values are noted in the graph if significance is observed.

Supplementary Figure 8: Reduced Aspartate/ Glutamate abundance impairs size of MPC overexpressing cells.

a-b. a) Representative bright field images of empty vector (EV) or MPC over-expressing (MPC+) HepG2 spheroids cultured with either 5 mM aspartate (Asp) or 5 mM glutamate (Glu). The scale bar represents 200 µm. **b)** Quantification of spheroid area is presented as mean ± s.d. of 30 technical replicates.

c-d. c) Representative bright field images of EV or MPC+ HepG2 spheroids with SLC1A3 overexpression (SLC13A+). The scale bar represents 200 µm. **d)** Quantification of spheroid area is presented as mean ± s.d. of 30 technical replicates. Western blots show the efficiency of MPC expression.

e. Quantification of d2GFP in EV or MPC+ HepG2 spheroids cultured under standard conditions or with three times the recommended concentration of non-essential amino acids cocktail (3X NEAA).

f-h. qRT-PCR showing **f)** *Mpc1*, **g)** *Mpc2*, and **h)** *Got2* transcripts from fat bodies of with control, MPC expression (MPC+), *Got2* knock down (*Got2*-KD), *Got2* knock down with MPC expression (MPC+, *Got2*-KD), *Got2* over-expression (*Got2*+), and *Got2* over-expression with MPC expression (MPC+, *Got2*+) normalized to *rp49* transcript abundance.

i. Quantification of the areas of EV and MPC+ HepG2 cells and HepG2 cells GOT2 knock out (GOT2-KO) with or without MPC expression. Data is presented as mean ± s.d. of five biological replicates, with 25 randomly selected cells analyzed per replicate. Western blots show the efficiency of GOT2 knockout using the two sgRNAs described.

j-k. **j)** Representative bright field images of EV, MPC+, GOT2+, and MPC+, GOT2+ HepG2 spheroids. The scale bar represents 200 µm. **k)** Quantification of spheroid areas is presented as mean ± s.d. of 30 technical replicates. Western blots show the efficiency of GOT2 over-expression.

Unpaired t-tests and one-way ANOVA tests were performed to evaluate the statistical significance of the data, and p-values are noted in the graph if significance is observed.

Figure 7: Increased mitochondrial pyruvate transport rewires metabolism and redox status to reduce protein synthesis and cell size in rat primary hepatocytes.

a. Western blot analysis of MPC overexpression in cultured rat primary hepatocytes.

b. Representative confocal images of rat primary hepatocytes expressing exogenous GFP or MPC. DIC images and DAPI staining of nuclei are also shown. Cell boundaries are marked with dotted lines. The scale bar represents 20 µm.

c. Quantification of the areas of GFP and MPC expressing primary hepatocytes. Data is presented as mean ± s.d. of six biological replicates, with 20 hepatocytes analyzed for GFP and MPC+.

d. Fluorescence intensity of puromycin-labeled nascent proteins in GFP and MPC+ primary hepatocytes. Data is presented as mean ± s.d. of six biological replicates, with 20 hepatocytes analyzed for each condition.

e. Quantification of glucose in the culture media of primary hepatocytes transfected with GFP or MPC constructs, conditioned with 20 mM lactate and 2 mM pyruvate for four hours. 10 µM UK5099 was used to inhibit MPC's downstream impact on gluconeogenesis. Data is presented as mean ± s.d. of 3 biological replicates.

f. $NADH/NAD^+$ ratios in the cytoplasmic and mitochondrial fractions of GFP or MPC+ primary hepatocytes. Data is presented as mean ± s.d. of three biological replicates.

g. Schematics illustrating the metabolic consequences of excess mitochondrial pyruvate in hepatocytes. Under normal conditions, mitochondrial pyruvate fuels the TCA cycle, maintaining redox balance and generating sufficient amino acids for cellular homeostasis. However, when mitochondrial pyruvate transport is increased and excess pyruvate is metabolized, both mitochondrial and cytoplasmic redox states are altered. This excess pyruvate enhances the activities of pyruvate carboxylase (PC), pyruvate dehydrogenase (PDH), and the TCA cycle, leading to an elevated $NADH/NAD^+$ ratio. The oxaloacetate produced by PC is converted into phosphoenolpyruvate via PEPCK2, promoting gluconeogenesis. This shift reduces the availability of aspartate and related amino acids necessary for protein synthesis, ultimately resulting in a reduction in cell size without impacting the canonical cell growth signaling pathways.

References

Alkan, H. F., Walter, K. E., Luengo, A., Madreiter-Sokolowski, C. T., Stryeck, S., Lau, A. N., Al-Zoughbi, W., Lewis, C. A., Thomas, C. J., Hoefler, G., Graier, W. F., Madl, T., Vander Heiden, M. G., & Bogner-Strauss, J. G. (2018). Cytosolic Aspartate Availability Determines Cell Survival When Glutamine Is Limiting. *Cell Metab*, *28*(5), 706-720 e706. https://doi.org/10.1016/j.cmet.2018.07.021

Amodeo, A. A., & Skotheim, J. M. (2016). Cell-Size Control. *Cold Spring Harb Perspect Biol*, *8*(4), a019083. https://doi.org/10.1101/cshperspect.a019083

Arrese, E. L., & Soulages, J. L. (2010). Insect fat body: energy, metabolism, and regulation. *Annu Rev Entomol*, *55*, 207-225. https://doi.org/10.1146/annurev-ento-112408-085356

Baena, E., Gandarillas, A., Vallespinos, M., Zanet, J., Bachs, O., Redondo, C., Fabregat, I., Martinez, A. C., & de Alboran, I. M. (2005). c-Myc regulates cell size and ploidy but is not essential for postnatal proliferation in liver. *Proc Natl Acad Sci U S A*, *102*(20), 7286-7291. https://doi.org/10.1073/pnas.0409260102

Baker, S. A., & Rutter, J. (2023). Metabolites as signalling molecules. *Nat Rev Mol Cell Biol*, *24*(5), 355-374. https://doi.org/10.1038/s41580-022-00572-w

Bensard, C. L., Wisidagama, D. R., Olson, K. A., Berg, J. A., Krah, N. M., Schell, J. C., Nowinski, S. M., Fogarty, S., Bott, A. J., Wei, P., Dove, K. K., Tanner, J. M., Panic, V., Cluntun, A., Lettlova, S., Earl, C. S., Namnath, D. F., Vazquez-Arreguin, K., Villanueva, C. J., . . . Rutter, J. (2020). Regulation of Tumor Initiation by the Mitochondrial Pyruvate Carrier. *Cell Metab*, *31*(2), 284-300 e287. https://doi.org/10.1016/j.cmet.2019.11.002

Birsoy, K., Wang, T., Chen, W. W., Freinkman, E., Abu-Remaileh, M., & Sabatini, D. M. (2015). An Essential Role of the Mitochondrial Electron Transport Chain in Cell Proliferation Is to Enable Aspartate Synthesis. *Cell*, *162*(3), 540-551. https://doi.org/10.1016/j.cell.2015.07.016

Bjorklund, M. (2019). Cell size homeostasis: Metabolic control of growth and cell division. *Biochim Biophys Acta Mol Cell Res*, *1866*(3), 409-417. https://doi.org/10.1016/j.bbamcr.2018.10.002

Bornstein, M. R., Tian, R., & Arany, Z. (2024). Human cardiac metabolism. *Cell Metab*, *36*(7), 1456-1481. https://doi.org/10.1016/j.cmet.2024.06.003

Bricker, D. K., Taylor, E. B., Schell, J. C., Orsak, T., Boutron, A., Chen, Y. C., Cox, J. E., Cardon, C. M., Van Vranken, J. G., Dephoure, N., Redin, C., Boudina, S., Gygi, S. P., Brivet, M., Thummel, C. S., & Rutter, J. (2012). A mitochondrial pyruvate carrier required for pyruvate uptake in yeast, Drosophila, and humans. *Science*, *337*(6090), 96-100. https://doi.org/10.1126/science.1218099

Chai, P., Lan, P., Li, S., Yao, D., Chang, C., Cao, M., Shen, Y., Ge, S., Wu, J., Lei, M., & Fan, X. (2022). Mechanistic insight into allosteric activation of human pyruvate carboxylase by acetyl-CoA. *Mol Cell*, *82*(21), 4116-4130 e4116. https://doi.org/10.1016/j.molcel.2022.09.033

Cluntun, A. A., Badolia, R., Lettlova, S., Parnell, K. M., Shankar, T. S., Diakos, N. A., Olson, K. A., Taleb, I., Tatum, S. M., Berg, J. A., Cunningham, C. N., Van Ry, T., Bott, A. J., Krokidi, A. T., Fogarty, S., Skedros, S., Swiatek, W. I., Yu, X., Luo, B., . . . Drakos, S. G. (2021). The pyruvate-lactate axis modulates cardiac hypertrophy and heart failure. *Cell Metab*, *33*(3), 629-648 e610. https://doi.org/10.1016/j.cmet.2020.12.003

Colombani, J., Raisin, S., Pantalacci, S., Radimerski, T., Montagne, J., & Leopold, P. (2003). A nutrient sensor mechanism controls Drosophila growth. *Cell*, *114*(6), 739-749. https://doi.org/10.1016/s0092-8674(03)00713-x

Dang, C. V. (1999). c-Myc target genes involved in cell growth, apoptosis, and metabolism. *Mol Cell Biol*, *19*(1), 1-11. https://doi.org/10.1128/MCB.19.1.1

DeBerardinis, R. J., & Thompson, C. B. (2012). Cellular metabolism and disease: what do metabolic outliers teach us? *Cell*, *148*(6), 1132-1144. https://doi.org/10.1016/j.cell.2012.02.032

Deliu, L. P., Ghosh, A., & Grewal, S. S. (2017). Investigation of protein synthesis in Drosophila larvae using puromycin labelling. *Biol Open*, *6*(8), 1229-1234. https://doi.org/10.1242/bio.026294

Edgar, B. A., & Orr-Weaver, T. L. (2001). Endoreplication cell cycles: more for less. *Cell*, *105*(3), 297-306. https://doi.org/10.1016/s0092-8674(01)00334-8

Fernandez-Caggiano, M., Kamynina, A., Francois, A. A., Prysyazhna, O., Eykyn, T. R., Krasemann, S., Crespo-Leiro, M. G., Vieites, M. G., Bianchi, K., Morales, V., Domenech, N., & Eaton, P. (2020). Mitochondrial pyruvate carrier abundance mediates pathological cardiac hypertrophy. *Nat Metab*, *2*(11), 1223-1231. https://doi.org/10.1038/s42255-020-00276-5

Ghosh-Choudhary, S., Liu, J., & Finkel, T. (2020). Metabolic Regulation of Cell Fate and Function. *Trends Cell Biol*, *30*(3), 201-212. https://doi.org/10.1016/j.tcb.2019.12.005

Ginzberg, M. B., Chang, N., D'Souza, H., Patel, N., Kafri, R., & Kirschner, M. W. (2018). Cell size sensing in animal cells coordinates anabolic growth rates and cell cycle progression to maintain cell size uniformity. *Elife*, *7*. https://doi.org/10.7554/eLife.26957

Gonzalez, A., & Hall, M. N. (2017). Nutrient sensing and TOR signaling in yeast and mammals. *EMBO J*, *36*(4), 397-408. https://doi.org/10.15252/embj.201696010

Gonzalez, S., & Rallis, C. (2017). The TOR Signaling Pathway in Spatial and Temporal Control of Cell Size and Growth. *Front Cell Dev Biol*, *5*, 61. https://doi.org/10.3389/fcell.2017.00061

Goodman, R. P., Markhard, A. L., Shah, H., Sharma, R., Skinner, O. S., Clish, C. B., Deik, A., Patgiri, A., Hsu, Y. H., Masia, R., Noh, H. L., Suk, S., Goldberger, O., Hirschhorn, J. N., Yellen, G., Kim, J. K., & Mootha, V. K. (2020). Hepatic NADH reductive stress underlies common variation in metabolic traits. *Nature*, *583*(7814), 122-126. https://doi.org/10.1038/s41586-020-2337-2

Gospodaryov, D. V., Strilbytska, O. M., Semaniuk, U. V., Perkhulyn, N. V., Rovenko, B. M., Yurkevych, I. S., Barata, A. G., Dick, T. P., Lushchak, O. V., & Jacobs, H. T. (2020). Alternative NADH dehydrogenase extends lifespan and increases resistance to xenobiotics in Drosophila. *Biogerontology*, *21*(2), 155-171. https://doi.org/10.1007/s10522-019-09849-8

Gratz, S. J., Ukken, F. P., Rubinstein, C. D., Thiede, G., Donohue, L. K., Cummings, A. M., & O'Connor-Giles, K. M. (2014). Highly specific and efficient CRISPR/Cas9-catalyzed homology-directed repair in Drosophila. *Genetics*, *196*(4), 961-971. https://doi.org/10.1534/genetics.113.160713

Gray, L. R., Sultana, M. R., Rauckhorst, A. J., Oonthonpan, L., Tompkins, S. C., Sharma, A., Fu, X., Miao, R., Pewa, A. D., Brown, K. S., Lane, E. E., Dohlman, A., Zepeda-Orozco, D., Xie, J., Rutter, J., Norris, A. W., Cox, J. E., Burgess, S. C., Potthoff, M. J., & Taylor, E. B. (2015). Hepatic Mitochondrial Pyruvate Carrier 1 Is Required for Efficient Regulation of Gluconeogenesis and Whole-Body Glucose Homeostasis. *Cell Metab*, *22*(4), 669-681. https://doi.org/10.1016/j.cmet.2015.07.027

Grewal, S. S. (2009). Insulin/TOR signaling in growth and homeostasis: a view from the fly world. *Int J Biochem Cell Biol*, *41*(5), 1006-1010. https://doi.org/10.1016/j.biocel.2008.10.010

Hatting, M., Tavares, C. D. J., Sharabi, K., Rines, A. K., & Puigserver, P. (2018). Insulin regulation of gluconeogenesis. *Ann N Y Acad Sci*, *1411*(1), 21-35. https://doi.org/10.1111/nyas.13435

Hausler, N., Browning, J., Merritt, M., Storey, C., Milde, A., Jeffrey, F. M., Sherry, A. D., Malloy, C. R., & Burgess, S. C. (2006). Effects of insulin and cytosolic redox state on glucose production pathways in the isolated perfused mouse liver measured by integrated 2H and 13C NMR. *Biochem J*, *394*(Pt 2), 465-473. https://doi.org/10.1042/BJ20051174

Henry, J. A., Couch, L. S., & Rider, O. J. (2024). Myocardial Metabolism in Heart Failure with Preserved Ejection Fraction. *J Clin Med*, *13*(5). https://doi.org/10.3390/jcm13051195

Herzig, S., Raemy, E., Montessuit, S., Veuthey, J. L., Zamboni, N., Westermann, B., Kunji, E. R., & Martinou, J. C. (2012). Identification and functional expression of the mitochondrial pyruvate carrier. *Science*, *337*(6090), 93-96. https://doi.org/10.1126/science.1218530

Holecek, M. (2023a). Aspartic Acid in Health and Disease. *Nutrients*, *15*(18). https://doi.org/10.3390/nu15184023

Holecek, M. (2023b). Roles of malate and aspartate in gluconeogenesis in various physiological and pathological states. *Metabolism*, *145*, 155614. https://doi.org/10.1016/j.metabol.2023.155614

Iritani, B. M., & Eisenman, R. N. (1999). c-Myc enhances protein synthesis and cell size during B lymphocyte development. *Proc Natl Acad Sci U S A*, *96*(23), 13180-13185. https://doi.org/10.1073/pnas.96.23.13180

Ito, K., Awano, W., Suzuki, K., Hiromi, Y., & Yamamoto, D. (1997). The Drosophila mushroom body is a quadruple structure of clonal units each of which contains a virtually identical set of neurones and glial cells. *Development*, *124*(4), 761-771. https://doi.org/10.1242/dev.124.4.761

Jitrapakdee, S., St Maurice, M., Rayment, I., Cleland, W. W., Wallace, J. C., & Attwood, P. V. (2008). Structure, mechanism and regulation of pyruvate carboxylase. *Biochem J*, *413*(3), 369-387. https://doi.org/10.1042/BJ20080709

Jokinen, M. J., & Luukkonen, P. K. (2024). Hepatic mitochondrial reductive stress in the pathogenesis and treatment of steatotic liver disease. *Trends Pharmacol Sci*, *45*(4), 319-334. https://doi.org/10.1016/j.tips.2024.02.003

Kast, A., Nishikawa, J., Yabe, T., Nanri, H., & Albert, H. (1988). Circadian rhythm of liver parameters (cellular structures, mitotic activity, glycogen and lipids in liver and serum) during three consecutive cycles in phenobarbital-treated rats. *Chronobiol Int*, *5*(4), 363-385. https://doi.org/10.3109/07420528809067782

Kiesel, V. A., Sheeley, M. P., Coleman, M. F., Cotul, E. K., Donkin, S. S., Hursting, S. D., Wendt, M. K., & Teegarden, D. (2021). Pyruvate carboxylase and cancer progression. *Cancer Metab*, *9*(1), 20. https://doi.org/10.1186/s40170-021-00256-7

Lang, F., Busch, G. L., Ritter, M., Volkl, H., Waldegger, S., Gulbins, E., & Haussinger, D. (1998). Functional significance of cell volume regulatory mechanisms. *Physiol Rev*, *78*(1), 247-306. https://doi.org/10.1152/physrev.1998.78.1.247

Li, X., Zhao, X., Fang, Y., Jiang, X., Duong, T., Fan, C., Huang, C. C., & Kain, S. R. (1998). Generation of destabilized green fluorescent protein as a transcription reporter. *J Biol Chem*, *273*(52), 34970-34975. https://doi.org/10.1074/jbc.273.52.34970

Lieu, E. L., Nguyen, T., Rhyne, S., & Kim, J. (2020). Amino acids in cancer. *Exp Mol Med*, *52*(1), 15-30. https://doi.org/10.1038/s12276-020-0375-3

Liu, S., Tan, C., Tyers, M., Zetterberg, A., & Kafri, R. (2022). What programs the size of animal cells? *Front Cell Dev Biol*, *10*, 949382. https://doi.org/10.3389/fcell.2022.949382

Lloyd, A. C. (2013). The regulation of cell size. *Cell*, *154*(6), 1194-1205. https://doi.org/10.1016/j.cell.2013.08.053

Lunt, S. Y., & Vander Heiden, M. G. (2011). Aerobic glycolysis: meeting the metabolic requirements of cell proliferation. *Annu Rev Cell Dev Biol*, *27*, 441-464. https://doi.org/10.1146/annurev-cellbio-092910-154237

McCommis, K. S., Chen, Z., Fu, X., McDonald, W. G., Colca, J. R., Kletzien, R. F., Burgess, S. C., & Finck, B. N. (2015). Loss of Mitochondrial Pyruvate Carrier 2 in the Liver Leads to Defects in Gluconeogenesis and Compensation via Pyruvate-Alanine Cycling. *Cell Metab*, *22*(4), 682-694. https://doi.org/10.1016/j.cmet.2015.07.028

McCommis, K. S., Kovacs, A., Weinheimer, C. J., Shew, T. M., Koves, T. R., Ilkayeva, O. R., Kamm, D. R., Pyles, K. D., King, M. T., Veech, R. L., DeBosch, B. J., Muoio, D. M.,

Gross, R. W., & Finck, B. N. (2020). Nutritional modulation of heart failure in mitochondrial pyruvate carrier-deficient mice. *Nat Metab*, *2*(11), 1232-1247. https://doi.org/10.1038/s42255-020-00296-1

Merker, M. P., Audi, S. H., Bongard, R. D., Lindemer, B. J., & Krenz, G. S. (2006). Influence of pulmonary arterial endothelial cells on quinone redox status: effect of hyperoxia-induced NAD(P)H:quinone oxidoreductase 1. *Am J Physiol Lung Cell Mol Physiol*, *290*(3), L607-619. https://doi.org/10.1152/ajplung.00302.2005

Metallo, C. M., & Vander Heiden, M. G. (2013). Understanding metabolic regulation and its influence on cell physiology. *Mol Cell*, *49*(3), 388-398. https://doi.org/10.1016/j.molcel.2013.01.018

Musselman, L. P., Fink, J. L., Ramachandran, P. V., Patterson, B. W., Okunade, A. L., Maier, E., Brent, M. R., Turk, J., & Baranski, T. J. (2013). Role of fat body lipogenesis in protection against the effects of caloric overload in Drosophila. *J Biol Chem*, *288*(12), 8028-8042. https://doi.org/10.1074/jbc.M112.371047

Pavlova, N. N., King, B., Josselsohn, R. H., Violante, S., Macera, V. L., Vardhana, S. A., Cross, J. R., & Thompson, C. B. (2020). Translation in amino-acid-poor environments is limited by tRNA(Gln) charging. *Elife*, *9*. https://doi.org/10.7554/eLife.62307

Petersen, M. C., Vatner, D. F., & Shulman, G. I. (2017). Regulation of hepatic glucose metabolism in health and disease. *Nat Rev Endocrinol*, *13*(10), 572-587. https://doi.org/10.1038/nrendo.2017.80

Reinke, H., & Asher, G. (2018). Liver size: Waning by day, Waxing by Night. *Hepatology*, *67*(1), 441-443. https://doi.org/10.1002/hep.29506

Rui, L. (2014). Energy metabolism in the liver. *Compr Physiol*, *4*(1), 177-197. https://doi.org/10.1002/cphy.c130024

Sanz, A., Soikkeli, M., Portero-Otin, M., Wilson, A., Kemppainen, E., McIlroy, G., Ellila, S., Kemppainen, K. K., Tuomela, T., Lakanmaa, M., Kiviranta, E., Stefanatos, R., Dufour, E., Hutz, B., Naudi, A., Jove, M., Zeb, A., Vartiainen, S., Matsuno-Yagi, A., . . . Jacobs, H. T. (2010). Expression of the yeast NADH dehydrogenase Ndi1 in Drosophila confers increased lifespan independently of dietary restriction. *Proc Natl Acad Sci U S A*, *107*(20), 9105-9110. https://doi.org/10.1073/pnas.0911539107

Saxton, R. A., & Sabatini, D. M. (2017). mTOR Signaling in Growth, Metabolism, and Disease. *Cell*, *168*(6), 960-976. https://doi.org/10.1016/j.cell.2017.02.004

Schell, J. C., Olson, K. A., Jiang, L., Hawkins, A. J., Van Vranken, J. G., Xie, J., Egnatchik, R. A., Earl, E. G., DeBerardinis, R. J., & Rutter, J. (2014). A role for the mitochondrial pyruvate carrier as a repressor of the Warburg effect and colon cancer cell growth. *Mol Cell*, *56*(3), 400-413. https://doi.org/10.1016/j.molcel.2014.09.026

Schell, J. C., Wisidagama, D. R., Bensard, C., Zhao, H., Wei, P., Tanner, J., Flores, A., Mohlman, J., Sorensen, L. K., Earl, C. S., Olson, K. A., Miao, R., Waller, T. C., Delker, D., Kanth, P., Jiang, L., DeBerardinis, R. J., Bronner, M. P., Li, D. Y., . . . Rutter, J. (2017). Control of intestinal stem cell function and proliferation by mitochondrial pyruvate metabolism. *Nat Cell Biol*, *19*(9), 1027-1036. https://doi.org/10.1038/ncb3593

Schmoller, K. M., & Skotheim, J. M. (2015). The Biosynthetic Basis of Cell Size Control. *Trends Cell Biol*, *25*(12), 793-802. https://doi.org/10.1016/j.tcb.2015.10.006

Shen, Y., Liu, W., Zuo, J., Han, J., & Zhang, Z. C. (2021). Protocol for visualizing newly synthesized proteins in primary mouse hepatocytes. *STAR Protoc*, *2*(3), 100616. https://doi.org/10.1016/j.xpro.2021.100616

Siess, E. A., Brocks, D. G., Lattke, H. K., & Wieland, O. H. (1977). Effect of glucagon on metabolite compartmentation in isolated rat liver cells during gluconeogenesis from lactate. *Biochem J*, *166*(2), 225-235. https://doi.org/10.1042/bj1660225

Sinturel, F., Gerber, A., Mauvoisin, D., Wang, J., Gatfield, D., Stubblefield, J. J., Green, C. B., Gachon, F., & Schibler, U. (2017). Diurnal Oscillations in Liver Mass and Cell Size

Accompany Ribosome Assembly Cycles. *Cell*, *169*(4), 651-663 e614. https://doi.org/10.1016/j.cell.2017.04.015

Stacpoole, P. W. (2017). Therapeutic Targeting of the Pyruvate Dehydrogenase Complex/Pyruvate Dehydrogenase Kinase (PDC/PDK) Axis in Cancer. *J Natl Cancer Inst*, *109*(11). https://doi.org/10.1093/jnci/djx071

Stine, Z. E., Walton, Z. E., Altman, B. J., Hsieh, A. L., & Dang, C. V. (2015). MYC, Metabolism, and Cancer. *Cancer Discov*, *5*(10), 1024-1039. https://doi.org/10.1158/2159-8290.CD-15-0507

Sugden, M. C., & Holness, M. J. (2011). The pyruvate carboxylase-pyruvate dehydrogenase axis in islet pyruvate metabolism: Going round in circles? *Islets*, *3*(6), 302-319. https://doi.org/10.4161/isl.3.6.17806

Sullivan, L. B., Gui, D. Y., Hosios, A. M., Bush, L. N., Freinkman, E., & Vander Heiden, M. G. (2015). Supporting Aspartate Biosynthesis Is an Essential Function of Respiration in Proliferating Cells. *Cell*, *162*(3), 552-563. https://doi.org/10.1016/j.cell.2015.07.017

Sullivan, L. B., Luengo, A., Danai, L. V., Bush, L. N., Diehl, F. F., Hosios, A. M., Lau, A. N., Elmiligy, S., Malstrom, S., Lewis, C. A., & Vander Heiden, M. G. (2018). Aspartate is an endogenous metabolic limitation for tumour growth. *Nat Cell Biol*, *20*(7), 782-788. https://doi.org/10.1038/s41556-018-0125-0

Tan, C., Ginzberg, M. B., Webster, R., Iyengar, S., Liu, S., Papadopoli, D., Concannon, J., Wang, Y., Auld, D. S., Jenkins, J. L., Rost, H., Topisirovic, I., Hilfinger, A., Derry, W. B., Patel, N., & Kafri, R. (2021). Cell size homeostasis is maintained by CDK4-dependent activation of p38 MAPK. *Dev Cell*, *56*(12), 1756-1769 e1757. https://doi.org/10.1016/j.devcel.2021.04.030

Tom Dieck, S., Muller, A., Nehring, A., Hinz, F. I., Bartnik, I., Schuman, E. M., & Dieterich, D. C. (2012). Metabolic labeling with noncanonical amino acids and visualization by chemoselective fluorescent tagging. *Curr Protoc Cell Biol*, *Chapter 7*, 7 11 11-17 11 29. https://doi.org/10.1002/0471143030.cb0711s56

Toshniwal, A. G., Gupta, S., Mandal, L., & Mandal, S. (2019). ROS Inhibits Cell Growth by Regulating 4EBP and S6K, Independent of TOR, during Development. *Dev Cell*, *49*(3), 473-489 e479. https://doi.org/10.1016/j.devcel.2019.04.008

Ugrankar-Banerjee, R., Tran, S., Bowerman, J., Kovalenko, A., Paul, B., & Henne, W. M. (2023). The fat body cortical actin network regulates Drosophila inter-organ nutrient trafficking, signaling, and adipose cell size. *Elife*, *12*. https://doi.org/10.7554/eLife.81170

van Riggelen, J., Yetil, A., & Felsher, D. W. (2010). MYC as a regulator of ribosome biogenesis and protein synthesis. *Nat Rev Cancer*, *10*(4), 301-309. https://doi.org/10.1038/nrc2819

Vander Heiden, M. G., Cantley, L. C., & Thompson, C. B. (2009). Understanding the Warburg effect: the metabolic requirements of cell proliferation. *Science*, *324*(5930), 1029-1033. https://doi.org/10.1126/science.1160809

Villalobos-Cantor, S., Barrett, R. M., Condon, A. F., Arreola-Bustos, A., Rodriguez, K. M., Cohen, M. S., & Martin, I. (2023). Rapid cell type-specific nascent proteome labeling in Drosophila. *Elife*, *12*. https://doi.org/10.7554/eLife.83545

Wang, X., Shen, X., Yan, Y., & Li, H. (2021). Pyruvate dehydrogenase kinases (PDKs): an overview toward clinical applications. *Biosci Rep*, *41*(4). https://doi.org/10.1042/BSR20204402

Wei, P., Bott, A. J., Cluntun, A. A., Morgan, J. T., Cunningham, C. N., Schell, J. C., Ouyang, Y., Ficarro, S. B., Marto, J. A., Danial, N. N., DeBerardinis, R. J., & Rutter, J. (2022). Mitochondrial pyruvate supports lymphoma proliferation by fueling a glutamate pyruvate transaminase 2-dependent glutaminolysis pathway. *Sci Adv*, *8*(39), eabq0117. https://doi.org/10.1126/sciadv.abq0117

Wei, Z., Liu, X., Cheng, C., Yu, W., & Yi, P. (2020). Metabolism of Amino Acids in Cancer. *Front Cell Dev Biol*, *8*, 603837. https://doi.org/10.3389/fcell.2020.603837

Weiss, R. C., Menezes, T. N., & McCommis, K. S. (2023). Metabolic Drivers and Rescuers of Heart Failure. *Mo Med*, *120*(5), 354-358. https://www.ncbi.nlm.nih.gov/pubmed/37841572

Xue, Y. W., Itoh, H., Dan, S., & Inoue, M. (2022). Gramicidin A accumulates in mitochondria, reduces ATP levels, induces mitophagy, and inhibits cancer cell growth. *Chem Sci*, *13*(25), 7482-7491. https://doi.org/10.1039/d2sc02024f

Yiew, N. K. H., & Finck, B. N. (2022). The mitochondrial pyruvate carrier at the crossroads of intermediary metabolism. *Am J Physiol Endocrinol Metab*, *323*(1), E33-E52. https://doi.org/10.1152/ajpendo.00074.2022

Yoo, H. C., Yu, Y. C., Sung, Y., & Han, J. M. (2020). Glutamine reliance in cell metabolism. *Exp Mol Med*, *52*(9), 1496-1516. https://doi.org/10.1038/s12276-020-00504-8

Zangari, J., Petrelli, F., Maillot, B., & Martinou, J. C. (2020). The Multifaceted Pyruvate Metabolism: Role of the Mitochondrial Pyruvate Carrier. *Biomolecules*, *10*(7). https://doi.org/10.3390/biom10071068

Zhang, S., Zatulovskiy, E., Arand, J., Sage, J., & Skotheim, J. M. (2022). The cell cycle inhibitor RB is diluted in G1 and contributes to controlling cell size in the mouse liver. *Front Cell Dev Biol*, *10*, 965595. https://doi.org/10.3389/fcell.2022.965595

Zhang, Y., Taufalele, P. V., Cochran, J. D., Robillard-Frayne, I., Marx, J. M., Soto, J., Rauckhorst, A. J., Tayyari, F., Pewa, A. D., Gray, L. R., Teesch, L. M., Puchalska, P., Funari, T. R., McGlauflin, R., Zimmerman, K., Kutschke, W. J., Cassier, T., Hitchcock, S., Lin, K., . . . Abel, E. D. (2020). Mitochondrial pyruvate carriers are required for myocardial stress adaptation. *Nat Metab*, *2*(11), 1248-1264. https://doi.org/10.1038/s42255-020-00288-1

Zheng, H., Yang, X., & Xi, Y. (2016). Fat body remodeling and homeostasis control in Drosophila. *Life Sci*, *167*, 22-31. https://doi.org/10.1016/j.lfs.2016.10.019

Zhu, J., & Thompson, C. B. (2019). Metabolic regulation of cell growth and proliferation. *Nat Rev Mol Cell Biol*, *20*(7), 436-450. https://doi.org/10.1038/s41580-019-0123-5

Author Information

Ashish G. Toshniwal
Department of Biochemistry, The University of Utah, Salt Lake City, United States

Contribution
Conceptualization, Data curation, Formal analysis, Validation, Investigation, Visualization, Methodology, Writing – original draft, Writing – review and editing

Geanette Lam
Department of Biochemistry, The University of Utah, Salt Lake City, United States
Contribution
Methodology

Ahmad A Cluntun
Department of Biochemistry, The University of Utah, Salt Lake City, United States
Present address: Department of Biochemistry & Molecular Biology, Rutgers Robert Wood Johnson Medical School, Piscataway, NJ 08854
Contribution
Investigation, Methodology

Alex J. Bott
Department of Biochemistry, The University of Utah, Salt Lake City, United States
Contribution
Investigation, Methodology

Hyuck-Jin Nam
Department of Human Genetics, University of Utah, Salt Lake City, UT 84132, USA
Contribution
Methodology

Rachel Skabelund
Department of Biochemistry, The University of Utah, Salt Lake City, United States
Contribution
Methodology

Dona R. Wisidagama,
Department of Human Genetics, University of Utah, Salt Lake City, UT 84132, USA
Contribution
Investigation

Carl S. Thummel
Department of Human Genetics, University of Utah, Salt Lake City, UT 84132, USA
Contribution
Conceptualization, Resources, Supervision, Funding acquisition, Writing – review and editing

Jared Rutter
1. Department of Biochemistry, The University of Utah, Salt Lake City, United States
2. Howard Hughes Medical Institute, University of Utah, Salt Lake City, United States

Contribution
Conceptualization, Resources, Supervision, Funding acquisition, Writing – original draft, Project administration, Writing – review and editing
Lead contact

Funding
American Heart Association (24POST1201210)

Ashish G Toshniwal
National Institutes of Health (K00CA212445)
Alex J. Bott
National Institutes of Health (1K99HL168312-01)
Ahmad A Cluntun
National Institutes of Health (R01CA228346)
Carl Thummel
Howard Hughes Medical Institute and National Institutes of Health (R01CA228346)
Jared Rutter
The funders had no role in study design, data collection and interpretation, or the decision to submit the work for publication.

Acknowledgements

We thank the University of Utah core facilities, especially James Cox, PhD, at the Metabolomics core, Li Ying, PhD, at the Metabolic Phenotyping core, James Marvin, PhD, at the Flow Cytometry Core, Brian Dalley, PhD, at the High-Throughput Genomics Core, and the DNA/Peptide Synthesis Core. We thank members of the Rutter lab for discussion and feedback on the manuscript. Several of the figures were created with BioRender.com. This study was supported by 24POST1201210 to AGT; K00CA212445 to AJB; 1K99HL168312-01 To AAC, R01 CA228346 to CT and JR. JR is an Investigator of the Howard Hughes Medical Institute.

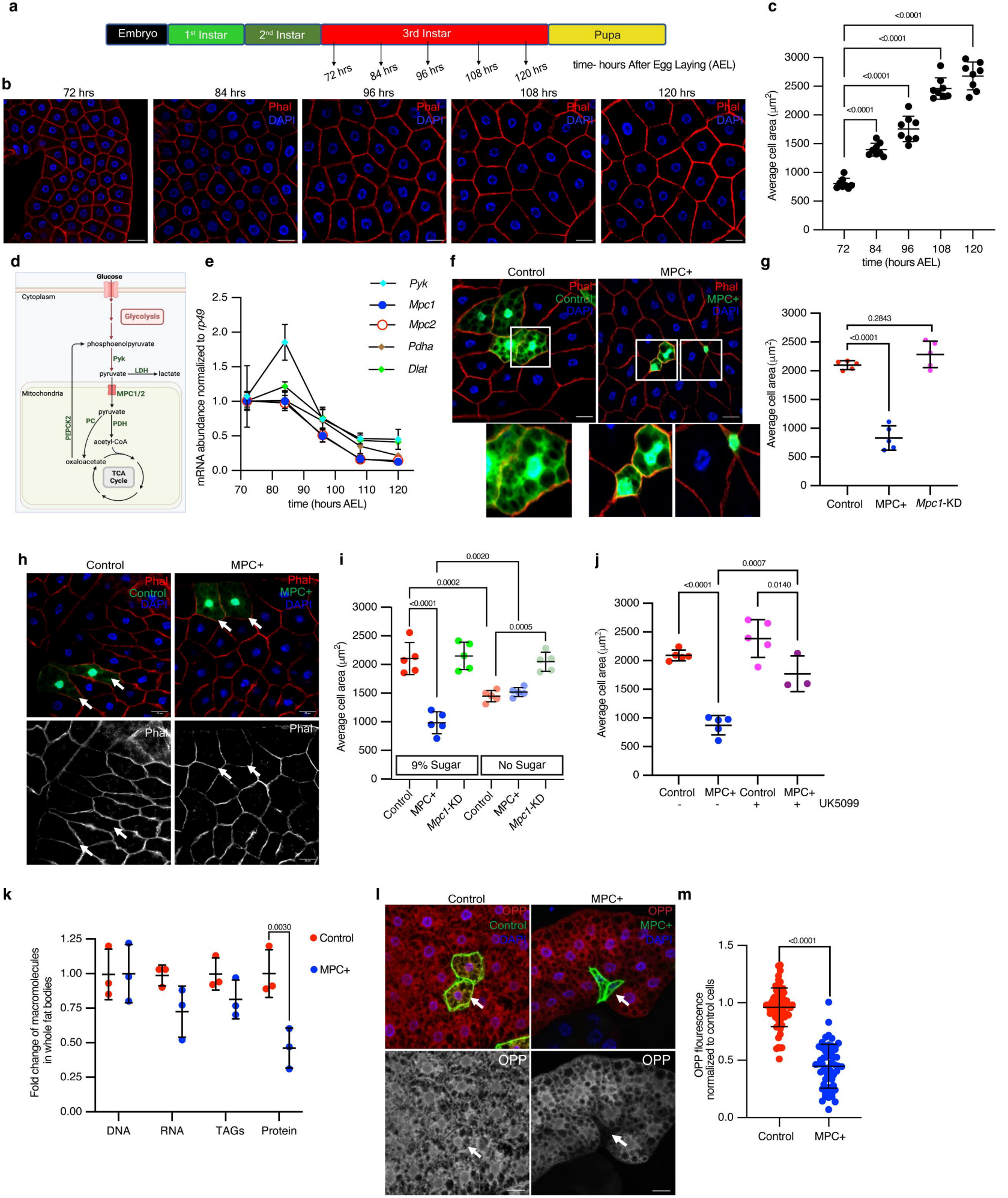

Figure 1: Increased mitochondrial pyruvate transport reduces size of *Drosophila* fat body cells

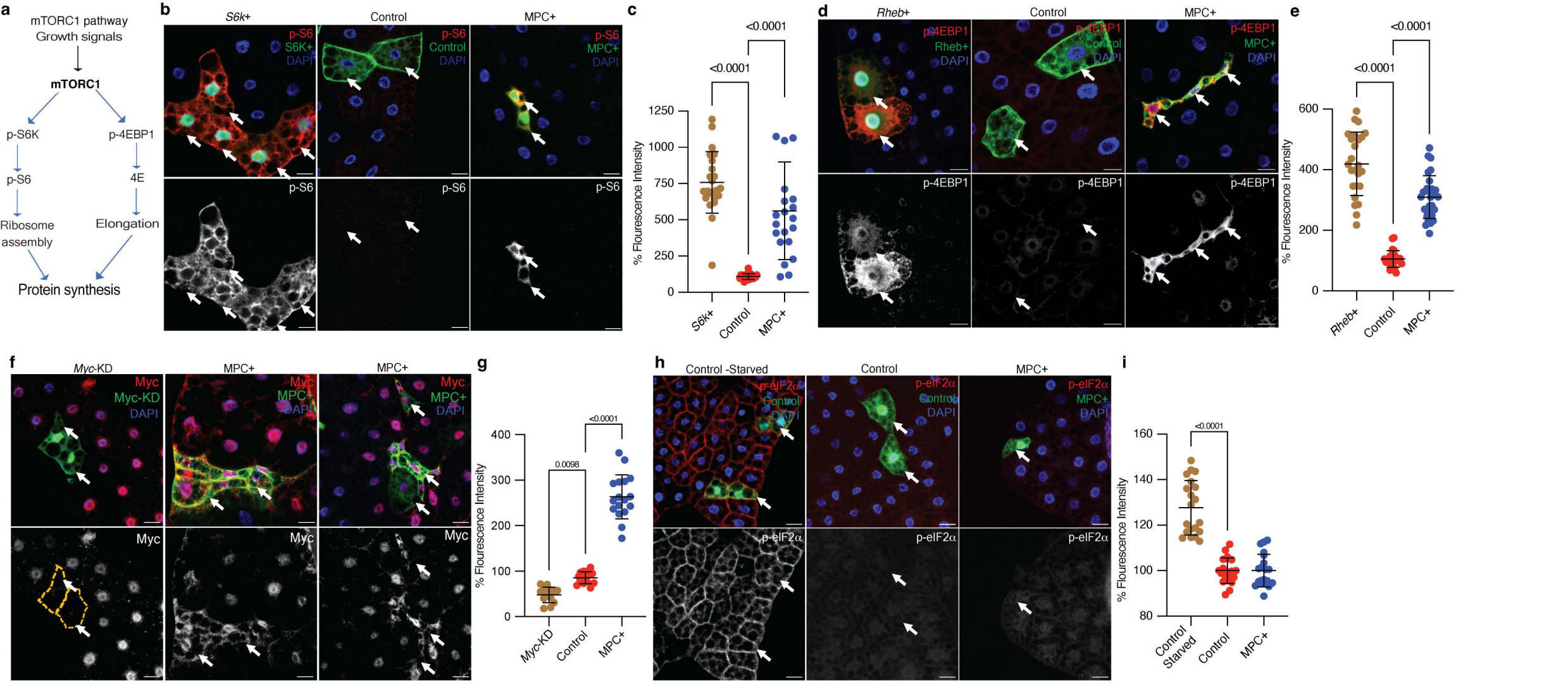

Figure 2 – mTORC1 and Myc pathways are hyperactivated in MPC expressing fat body cells.

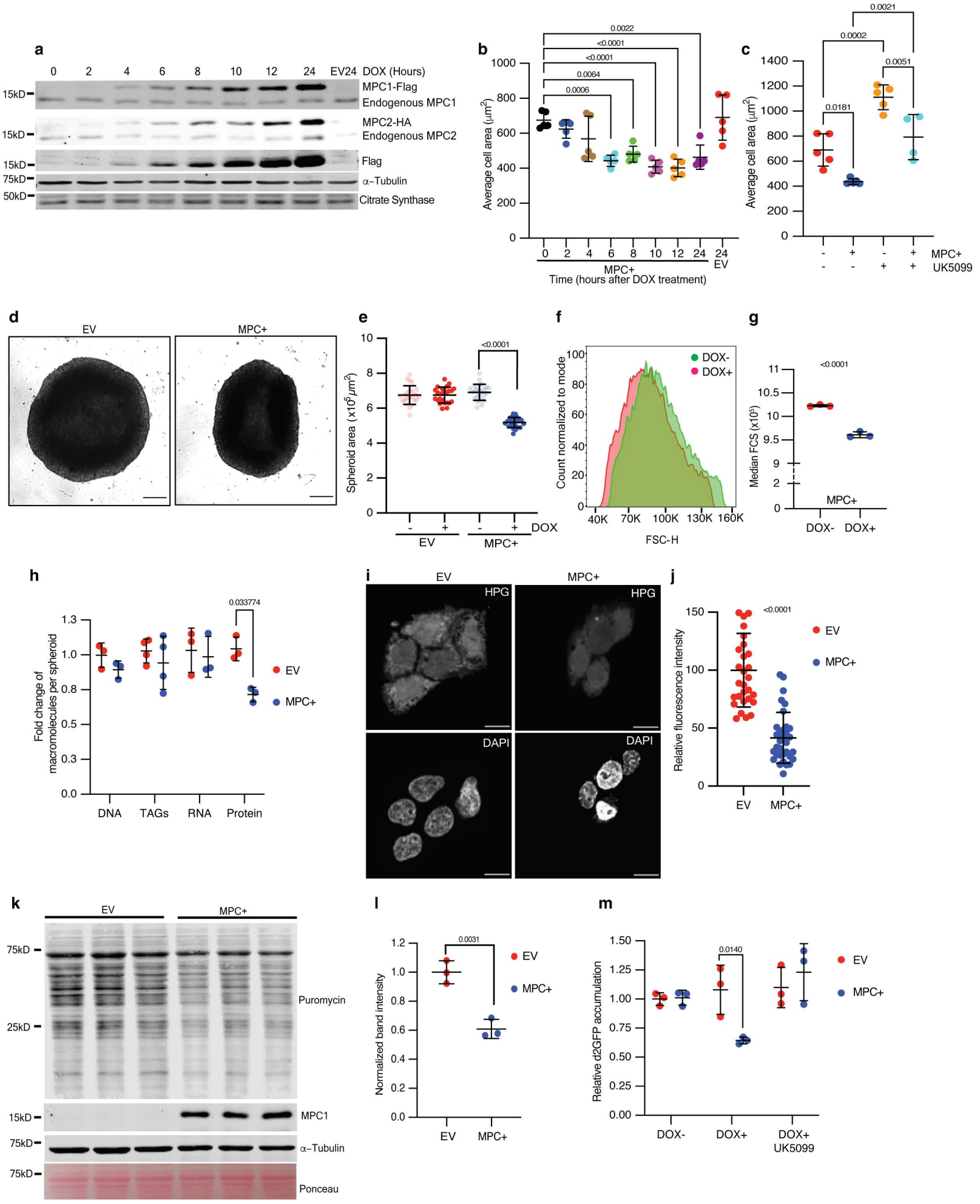

Figure 3 – Increased mitochondrial pyruvate transport reduces size of HepG2 spheroids.

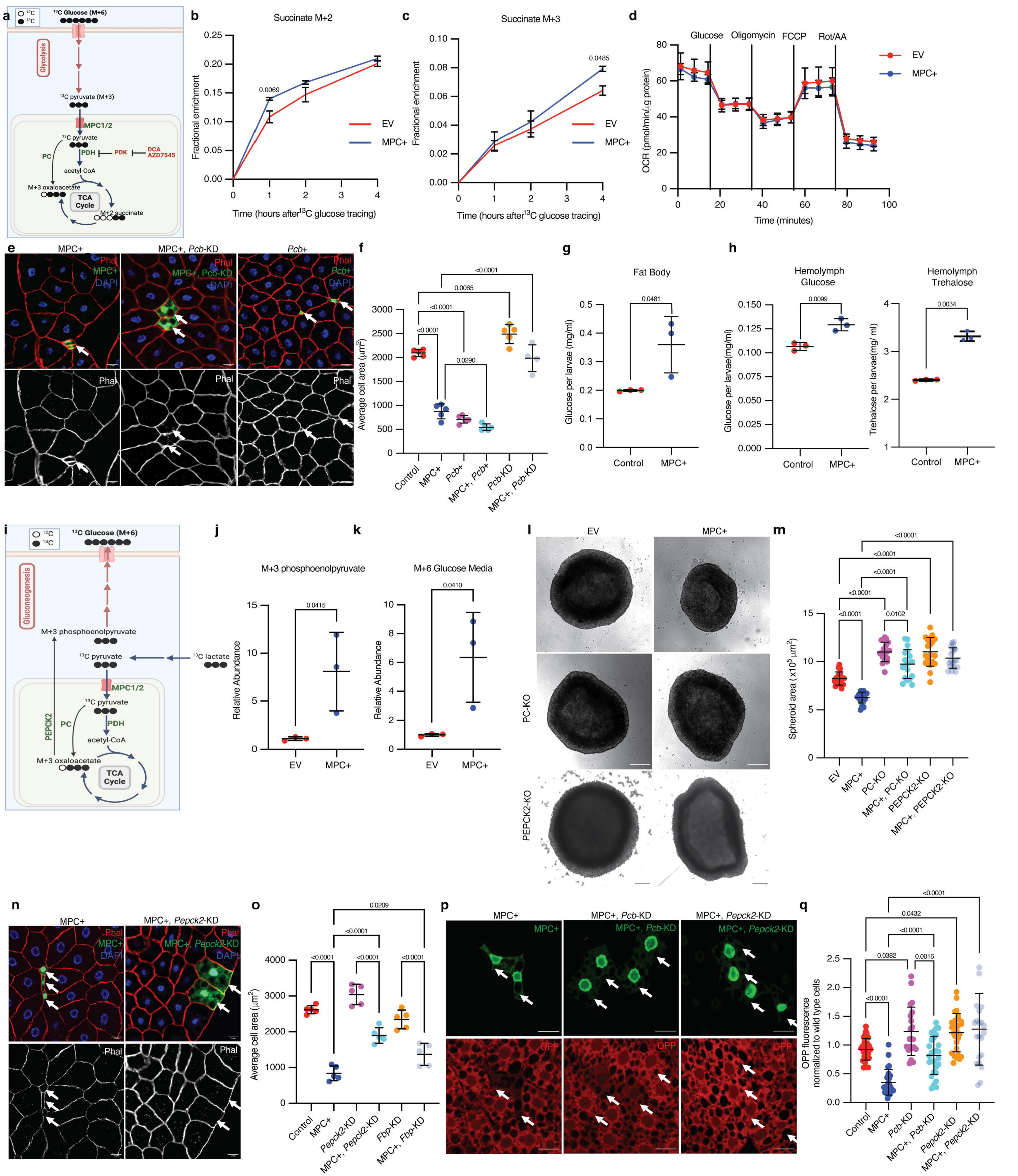

Figure 4: Increased mitochondrial pyruvate metabolism promotes gluconeogenesis via pyruvate carboxylase to suppress protein synthesis

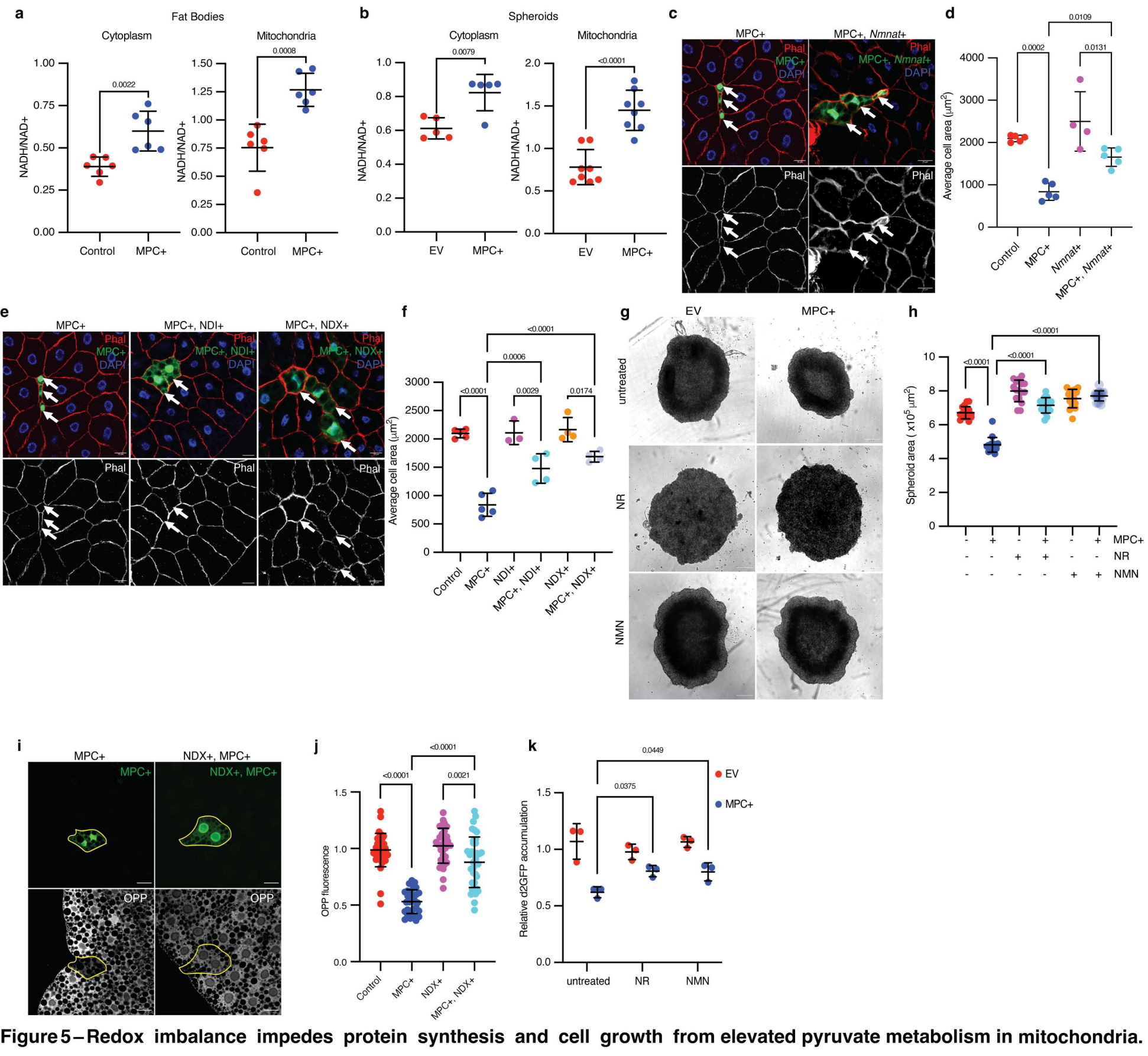

Figure 5 – Redox imbalance impedes protein synthesis and cell growth from elevated pyruvate metabolism in mitochondria.

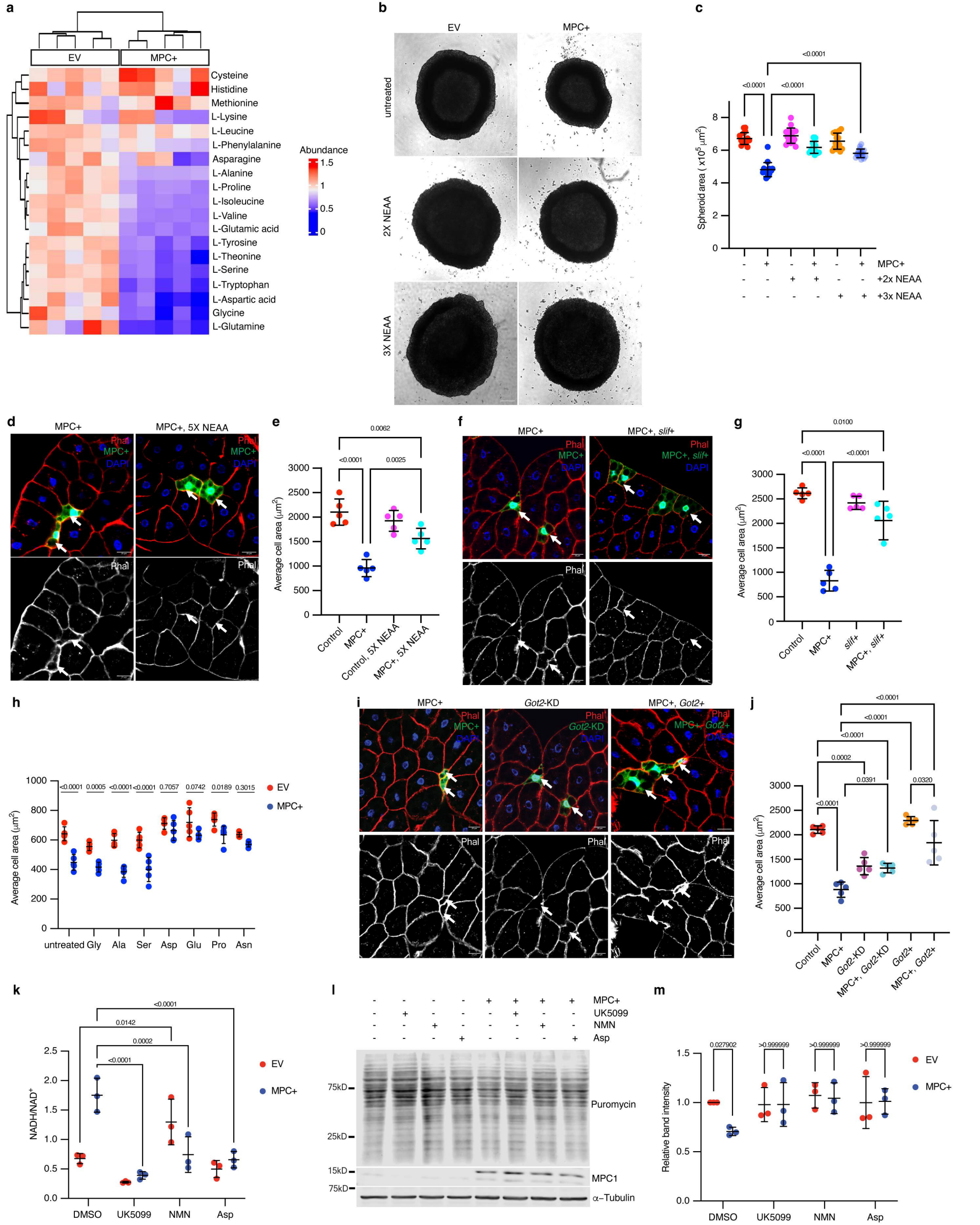

Figure 6 – Reduced amino acid abundance impairs size of MPC-expressing cells

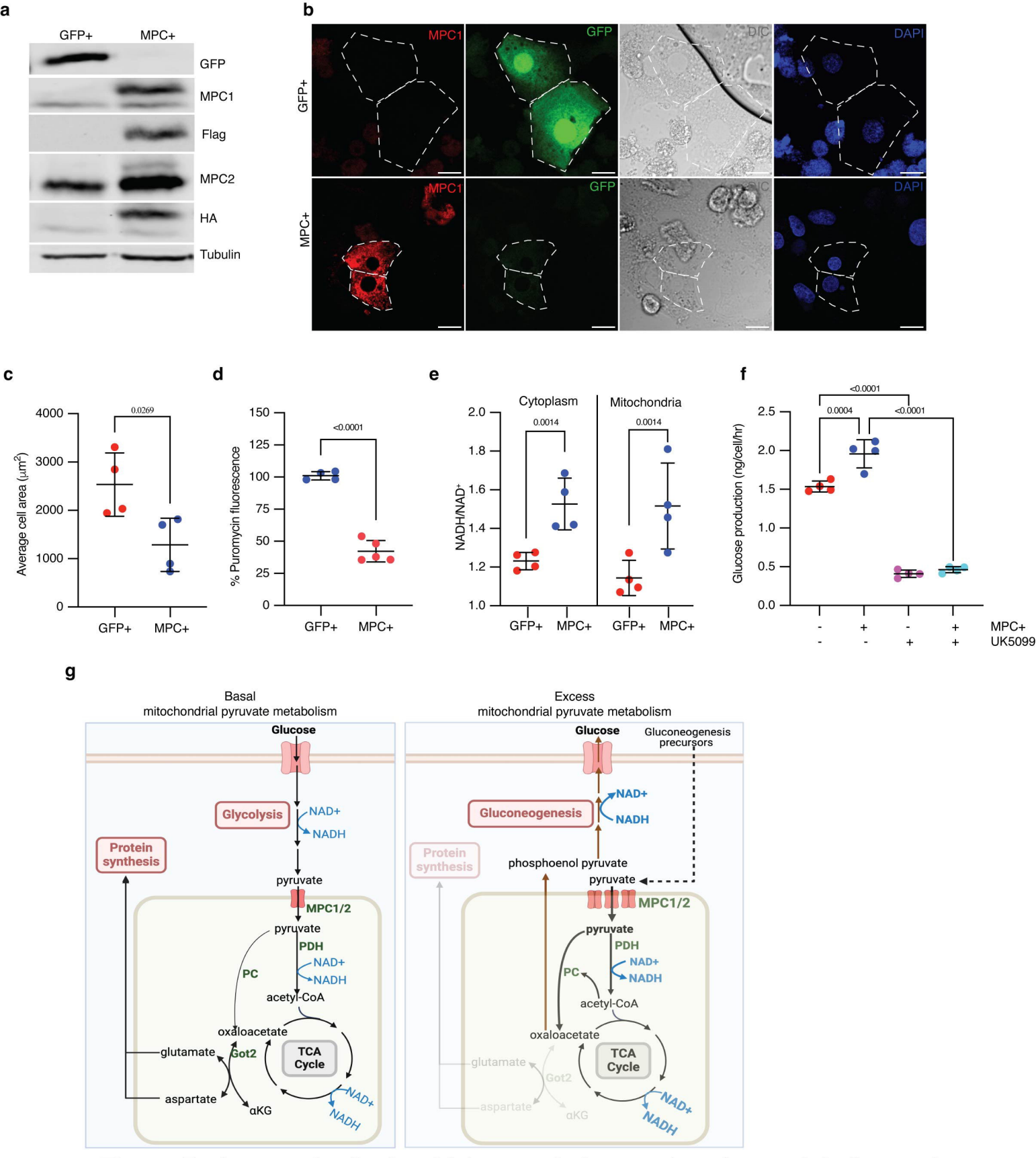

Figure 7– Increased mitochondrial pyruvate transport rewires metabolism and redox status to reduce protein synthesis and cell size in rat primary hepatocytes